Wang, Y., Feng, C., Wang, X., Zhao, Z., Romero, C. S., Dong, Y. & Yang, J. (2019). Nonlinear static and dynamic responses of graphene platelets reinforced composite beam with dielectric permittivity. *Applied Mathematical Modelling, 71*, 298–315.

DOI: 10.1016/j.apm.2019.02.025

Nonlinear Bending and Forced Vibration of Graphene Platelets Reinforced Composite Beam with Dielectric Permittivity

Yu Wang[1], Chuang Feng[*, 1], Xinwei Wang[2], Zhan Zhao[1], Carlos Santiuste Romero[3], Youheng Dong[1], Jie Yang [1, †]

[1]School of Engineering, RMIT University, Bundoora, VIC 3083 Australia

[2]State Key Laboratory of Mechanics and Control of Mechanical Structures, Nanjing University of Aeronautics and Astronautics, Nanjing, PR China

[3]Department of Continuum Mechanics and Structural Analysis, Universidad Carlos III de Madrid, Avda de la Universidad 30, 28911 Leganés, Spain

Abstract

Nonlinear bending and forced vibration of graphene platelets (GPLs) reinforced composite (GPLRC) beam with dielectric permittivity are investigated. The tensile modulus and dielectric permittivity as required for structural analysis are obtained by using effective-medium theory (EMT) while Poisson's ratio and mass density are evaluated by rule of mixture. Based on Timoshenko beam theory, governing equations for nonlinear bending and forced vibration of the GPLRC beam are established and numerically solved through differential quadrature method (DQM). The dependency of the structural behaviours of the GPLRC beams on the attributes of GPL, applied external loading and electrical field are comprehensively studied. The analysis demonstrates that the performances of the GPLRC beam can be designed and actively tuned through adjusting several parameters. The bending and vibration behaviours of the beam are sensitive to smaller beam thickness, larger GPL aspect ratio and electrical voltage. Snap-through behaviour is observed for the bending and vibration of the composite beam within the involved AC frequency range. Reasons underlying the above observations are analyzed and discussed to increasingly understand the structural behaviours of graphene reinforced composite structures with dielectric property.

Corresponding Authors

[*] E-mail: chuang.feng@rmit.edu.au (C. Feng);

[†] Email: j.yang@rmit.edu.au (J. Yang)

Keywords: Forced vibration; Dielectric beam; Differential quadrature method; Effective-medium theory

1. Introduction

Materials with dielectric properties, which are named as high-κ materials [1-3], have demonstrated great potential in developing smart materials and structures for various engineering applications. This is attributed to their unique capability of active tuning of material properties and structure behaviours after manufacturing. Certain polymers, such as dielectric elastomer [4-7], have been proved as suitable high-κ candidates for various smart structures owning to their tunable attributes, flexibility, easy processability and low prices. However, these pure polymers' dielectric constant is usually not sufficiently large, which has significantly restricted the application spectrum of these polymer materials. To address this restriction, the dispersion of conductive particles, including carbon black (CB) [8, 9] and carbon nanotubes (CNTs) [10-12] into polymer matrix has been evidenced as an effective solution to develop composites with significantly improved dielectric properties.

Recently, graphene and graphene-derived materials, such as graphene platelet (GPL) and graphene oxide (GO), have been regarded as effective additives for polymer matrix to develop high-κ composites [13-15]. This interest stems from their significant reinforcing effect in the mechanical and physical performances. For instance, an addition of 0.04 wt% of graphene into polymer improves the fracture toughness and energy by 150% and 240%, respectively, compared to those of pristine epoxy [16]. Rafiee et al. [17] found the bulking resistance of epoxy would grow by 52% with a loading of 0.1 wt% of GPL. By adding 1.8 vol% of fully exfoliated graphene [18], the tensile modulus of Polyvinyl alcohol (PVA) composites can be improved by 10-folds. By using atomistic modelling, Rahman and Haque [19] and Sun et al. [20] also observed remarkable increase in the elastic properties of the graphene reinforced nanocomposites. The prediction by micromechanics models [21-24] also verified the reinforcing effects of graphene fillers on the mechanical properties of the nanocomposites. In addition to mechanical properties, Fan et al.'s [15] experiments demonstrated that adding 1.77 vol% of graphene into polyvinylidene fluoride (PVDF), the dielectric constant can reach as high as 7940 at 100 Hz. He et al. [25] manufactured PVDF nanocomposites with a loading of 1.01 vol% of GPL and observed that the dielectric constant can be more than 200 and 2700 at 1000 Hz and 100 Hz of AC (Alternating Current) frequency, respectively. Chen et al.'s [14] examination evidenced the dielectric permittivity of graphene/polymer nanocomposites is five times larger than that of pure polymer. In addition to experiments, Xia et al.'s [26] developed model, which was validated by comparing with experiments, also perceived obvious enhancement in dielectric permittivity of graphene reinforced polymer nanocomposites.

Apart from the efforts on characterizing and predicting the material properties of graphene reinforced nanocomposites, researches have been working on analysing structural performances of graphene reinforced composite components, including beams [27-32], plates [33-38] and shells [39-42]. Their results showed that the bending, vibration and buckling performances of these structures can be considerably improved by adding graphene and its derivatives as reinforcing fillers into polymers. Although plenty of work has been carried out on graphene reinforced composite structures, most of the previous work is focused on structural behaviours without considering the intrinsic dielectric attributes of the graphene reinforced nanocomposites. However, taking the advantages of the dielectric properties of these composites is essential for developing smart structures whereas limited work has been found on such topic despite of importance and great potential for engineering application.

Therefore, the present work will be the first concentration on nonlinear bending and forced vibration behaviours of graphene reinforced composite beam with considering the dielectric property of the composite material. For case study, PVDF and GPL are chosen as constituent components for the composite beam. Fig. 1 shows the GPL reinforced composite (GPLRC) beam with applied electrical voltage. It should be noted that the beam's top and bottom surfaces are coated with conductive paste serving as the compliant electrodes to accommodate the applied electrical voltage. Effective-medium theory (EMT) and rule of mixture will be employed to calculate the composite's material properties as required for structural analysis. Parametric study on the bending and forced vibration of the GPLRC beam is conducted through numerically solving the governing equations, which are derived by Timoshenko beam theory taking account of von Kármán geometrical nonlinearity.

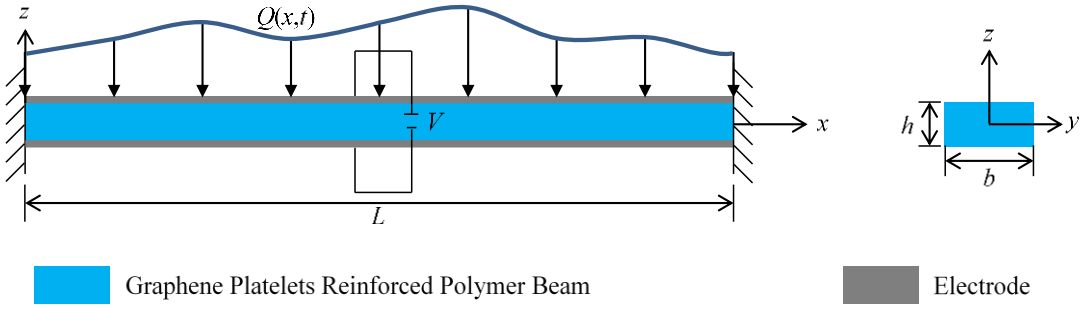

Fig. 1. Schematic configuration of GPLRC beam.

2. Effective material properties of GPLRC

Prior to structural analysis, the material properties of the GPLRC as required need to be determined. For GPLRC with randomly and uniformly dispersed reinforcing fillers, its effective Poisson's ratio and mass density can be estimated by rule of mixture rule as

$$\nu_{\mathrm{e}} = \varphi_{\mathrm{m}}\nu_{\mathrm{m}} + \varphi_{\mathrm{f}}\nu_{\mathrm{f}},\ \rho_{\mathrm{e}} = \varphi_{\mathrm{m}}\rho_{\mathrm{m}} + \varphi_{\mathrm{f}}\rho_{\mathrm{f}} \tag{1}$$

where the subscripts "m", "f" and "e" refer to polymer matrix, reinforcing fillers and effective composite, respectively, and ν, ρ and φ refer to Poisson's ratio, mass density and volume fraction, respectively.

Regarding to the elastic properties of GPLRC, Halpin-Tsai formula has been used as an effective method for prediction [43]. Apart from elastic modulus, dielectric permittivity of the GPLRC also needs to be determined. However, using Halpin-Tsai equation to derive composites' dielectric permittivity with capturing the underlying physical mechanisms is challenging. Therefore, in this paper, EMT is introduced and adopted to evaluate the effective elastic modulus together with the dielectric permittivity of GPLRC. According to Maxwell's approach [44] of far field matching, the field of the homogeneous GPLRC can be determined as

$$\boldsymbol{T}_{\mathrm{e}} = \sum_{i=1}^{n} \varphi_i \boldsymbol{T}_i \tag{2}$$

where φ_i and $\boldsymbol{T}_i$ denote the volume fraction and the field of the ith scattered constituent component at far distance, respectively. Selecting a reference medium, the filed $\boldsymbol{T}_i$ can be written as

$$\boldsymbol{T}_i = \left[\left(\boldsymbol{L}_i - \boldsymbol{L}_{\mathrm{r}} \right)^{-1} + \boldsymbol{S}_i \boldsymbol{L}_{\mathrm{r}}^{-1} \right]^{-1} \tag{3}$$

where $\boldsymbol{L}_i$ and $\boldsymbol{S}_i$ are the moduli and Eshelby's tensors of the ith constituent component, respectively, and $\boldsymbol{L}_{\mathrm{r}}$ denotes the moduli tensor of the reference medium. Particularly, selecting effective medium itself as reference medium, i.e. $L_r = L_{\mathrm{e}}$, Eq. (2) becomes the expression for EMT as

$$\sum_{i=1}^{n} \varphi_i \left[\left(\boldsymbol{L}_i - \boldsymbol{L}_{\mathrm{e}} \right)^{-1} + \boldsymbol{S}_i \boldsymbol{L}_{\mathrm{e}}^{-1} \right]^{-1} = 0 \tag{4}$$

When constituent components are randomly and uniformly distributed in the effective medium, we can average the term over all orientations to cast Eq. (4) as

$$\sum_{i=1}^{n} \varphi_i \left\langle \left[\left(\boldsymbol{L}_i - \boldsymbol{L}_{\mathrm{e}} \right)^{-1} + \boldsymbol{S}_i \boldsymbol{L}_{\mathrm{e}}^{-1} \right]^{-1} \right\rangle = 0 \tag{5}$$

where < > denotes term averaging. For two-phase GPLRC composites, Eq. (5) can be written as

$$\varphi_{\mathrm{m}} \left\langle \left[\left(\boldsymbol{L}_{\mathrm{m}} - \boldsymbol{L}_{\mathrm{e}} \right)^{-1} + \boldsymbol{S}_{\mathrm{m}} \boldsymbol{L}_{\mathrm{e}}^{-1} \right]^{-1} \right\rangle + \varphi_{\mathrm{f}} \left\langle \left[\left(\boldsymbol{L}_{\mathrm{f}} - \boldsymbol{L}_{\mathrm{e}} \right)^{-1} + \boldsymbol{S}_{\mathrm{f}} \boldsymbol{L}_{\mathrm{e}}^{-1} \right]^{-1} \right\rangle = 0 \tag{6}$$

Considering isotropic attributes of graphene reinforced composites, Eq. (6) becomes a scalar equation after averaging, i.e.

$$\varphi_{\mathrm{m}} \frac{L_{\mathrm{m}} - L_{\mathrm{e}}}{L_{\mathrm{m}} + (1/3)\left(L_{\mathrm{m}} - L_{\mathrm{e}} \right)} + \frac{1}{3} \varphi_{\mathrm{f}} \sum_{k=1}^{3} \frac{L_k - L_{\mathrm{e}}}{L_{\mathrm{e}} + S_{kk} \left(L_k - L_{\mathrm{e}} \right)} = 0 \tag{7}$$

where L_k (k = 1, 2, 3) is the moduli component of GPL filler in its local coordinate system.

2.1. Effective dielectric permittivity

The moduli tensors in Eq. (7) can be electrical conductivity of the effective medium. Substituting the corresponding moduli tensors, one can have

$$\varphi_{\mathrm{m}} \frac{\sigma_{\mathrm{m}}^{*} - \sigma_{\mathrm{e}}^{*}}{\sigma_{\mathrm{e}}^{*} + (1/3)\left(\sigma_{\mathrm{m}}^{*} - \sigma_{\mathrm{e}}^{*} \right)} + \frac{1}{3} \varphi_{\mathrm{f}} \sum_{k=1}^{3} \frac{\sigma_k^{*} - \sigma_{\mathrm{e}}^{*}}{\sigma_{\mathrm{e}}^{*} + S_{kk} \left(\sigma_k^{*} - \sigma_{\mathrm{e}}^{*} \right)} = 0 \tag{8}$$

where σ^* denote complex electrical conductivity. It consists of two parts, i.e. $\sigma^* = \sigma + 2\pi f_{\mathrm{AC}} \varepsilon j$, wherein σ is the DC (direct current) conductivity and the second imaginary term is the AC conductivity with f_{AC} being AC frequency of electrical field and ε the dielectric permittivity of the material.

Treating GPLs as reinforcing fillers with thin oblate spheroid shape [45], the elements of Eshelby's tensor used in Eq. (8) can be expressed as [46]

$$S = S_{11} = S_{22} = \frac{\alpha}{2\left(1-\alpha^2\right)^{3/2}}\left[\arccos\alpha - \alpha\left(1-\alpha^2\right)^{1/2}\right]$$
$$S_{33} = 1 - 2S_{22} \tag{9}$$

where $\alpha = t_{\mathrm{GPL}}/D_{\mathrm{GPL}}$ denotes GPL's thickness-to-diameter ratio with t_{GPL} being the thickness and D_{GPL} being the diameter.

To capture the imperfect bonding/interaction between reinforcements and matrix, an interphase surrounding the reinforcements is usually introduced [47, 48]. According to [49], the effective electrical conductivity and dielectric permittivity of the coated reinforcing fillers, i.e. $\sigma_k^{(\mathrm{c})}$ and $\varepsilon_k^{(\mathrm{c})}$, can be approximated as

$$\begin{cases} \sigma_k^{(\mathrm{c})} = \sigma_0^{(\mathrm{int})}\left[1 + \dfrac{\left(1-\varphi_{\mathrm{int}}\right)\left(\sigma_k - \sigma_0^{(\mathrm{int})}\right)}{\varphi_{\mathrm{int}} S_{kk}\left(\sigma_k - \sigma_0^{(\mathrm{int})}\right) + \sigma_0^{(\mathrm{int})}}\right] \\ \varepsilon_k^{(\mathrm{c})} = \varepsilon_0^{(\mathrm{int})}\left[1 + \dfrac{\left(1-\varphi_{\mathrm{int}}\right)\left(\varepsilon_k - \varepsilon_0^{(\mathrm{int})}\right)}{\varphi_{\mathrm{int}} S_{kk}\left(\varepsilon_k - \varepsilon_0^{(\mathrm{int})}\right) + \varepsilon_0^{(\mathrm{int})}}\right] \end{cases} \quad k = 1, 2, 3 \tag{10}$$

where $\sigma_0^{(\mathrm{int})}$ and $\varepsilon_0^{(\mathrm{int})}$ correspond to the interphase's electrical conductivity and dielectric permittivity, respectively. All the electrical conductivity and dielectric permittivity of the GPL fillers involved in Eq. (8) should be substituted by the ones in Eq. (10). φ_{int} in Eq. (10) denotes the volume fraction of the interphase in the coated GPL, which is

$$\varphi_{\mathrm{int}} = 1 - \frac{\dfrac{4}{3}\pi\left(\dfrac{t_{\mathrm{GPL}}}{2}\right)\left(\dfrac{D_{\mathrm{GPL}}}{2}\right)\left(\dfrac{D_{\mathrm{GPL}}}{2}\right)}{\dfrac{4}{3}\pi\left(\dfrac{t_{\mathrm{GPL}}}{2} + t_{\mathrm{int}}\right)\left(\dfrac{D_{\mathrm{GPL}}}{2} + t_{\mathrm{int}}\right)\left(\dfrac{D_{\mathrm{GPL}}}{2} + t_{\mathrm{int}}\right)} \tag{11}$$

where t_{int} is the thickness of the interphase.

It is easily understood that when more reinforcing fillers are dispersed, the average distance between adjacent fillers will decrease, leading to enhanced probability of interfacial electron hopping and MWS polarization. To capture such process of enhancement, $\sigma_0^{(\mathrm{int})}$ and $\varepsilon_0^{(\mathrm{int})}$, in Eq. (10) can be modified as [26]

$$\begin{cases}\sigma_{\text{static}}^{(\text{int})}=\sigma_{0}^{(\text{int})}\Big/\tau\left(\varphi_{\text{f}},\varphi_{\text{f}}^{*},\gamma_{\text{static}}^{\sigma}\right)\\ \varepsilon_{\text{static}}^{(\text{int})}=\varepsilon_{0}^{(\text{int})}\Big/\tau\left(\varphi_{\text{f}},\varphi_{\text{f}}^{*},\gamma_{\text{static}}^{\varepsilon}\right)\end{cases}\tag{12}$$

wherein the subscript "static" represents the parameters' independence on AC frequency of the electrical field, φ_{f}^{*} denotes the percolation threshold of the GPL/polymer composites, and $\gamma_{\text{static}}^{\sigma}$ and $\gamma_{\text{static}}^{\varepsilon}$ are the scale factors describing electron hopping and MWS polarization, respectively. $\tau\left(\varphi_{\text{f}},\varphi_{\text{f}}^{*},\gamma_{\text{static}}^{\sigma}\right)$ in Eq. (12) is a function written as [26, 49-51]

$$\tau\left(\varphi_{\text{f}},\varphi_{\text{f}}^{*},\gamma\right)=\frac{F\left(1,\varphi_{\text{f}}^{*},\gamma\right)-F\left(\varphi_{\text{f}},\varphi_{\text{f}}^{*},\gamma\right)}{F\left(1,\varphi_{\text{f}}^{*},\gamma\right)-F\left(0,\varphi_{\text{f}}^{*},\gamma\right)}\tag{13}$$

where $F\left(\varphi_{\text{f}},\varphi_{\text{f}}^{*},\gamma\right)=\frac{1}{\pi}\arctan\left(\frac{\varphi_{\text{f}}-\varphi_{\text{f}}^{*}}{\gamma}\right)+\frac{1}{2}$ is Cauchy's cumulative probabilistic function.

Subjected to AC electrical loading, AC frequency can facilitate the interfacial tunneling and MWS polarization effects. Therefore, $\sigma_{\text{static}}^{(\text{int})}$ and $\varepsilon_{\text{static}}^{(\text{int})}$ are further modified as functions depending on AC frequency as [26, 52]

$$\begin{cases}\sigma_{\text{frequency}}^{(\text{int})}\left(f_{\text{AC}}\right)=\sigma_{\text{static}}^{(\text{int})}p\left(f_{\text{AC}}\right)\\ \varepsilon_{\text{frequency}}^{(\text{int})}\left(f_{\text{AC}}\right)=\varepsilon_{\text{inf}}^{(\text{int})}+\dfrac{\varepsilon_{\text{static}}^{(\text{int})}-\varepsilon_{\text{inf}}^{(\text{int})}}{1+f_{\text{AC}}^{2}t_{\varepsilon}^{2}}\end{cases}\tag{14}$$

where

$$\begin{cases}p\left(f_{\text{AC}}\right)=\dfrac{2\pi f_{\text{AC}}t_{\sigma}\arctan(2\pi f_{\text{AC}}t_{\sigma})}{\left[0.5\ln\left(1+\left(2\pi f_{\text{AC}}t_{\sigma}\right)^{2}\right)\right]^{2}+\arctan^{2}\left(2\pi f_{\text{AC}}t_{\sigma}\right)}\\ \varepsilon_{\text{inf}}^{(\text{int})}=\varepsilon_{0}^{(\text{int})}\Big/\tau\left(\varphi_{\text{f}},\varphi_{\text{f}}^{*},\gamma_{\text{inf}}^{\varepsilon}\right)\end{cases}\tag{15}$$

In Eqs. (14) and (15), t_σ is the characteristic time of electron tunneling, t_ε is the relaxation time of Debye theory, $\varepsilon_{\text{inf}}^{(\text{int})}$ is the interface's dielectric permittivity at infinite AC frequency and $\gamma_{\text{inf}}^{\varepsilon}$ is the scale factor denoting nanocapacitors formation at infinite AC frequency.

Choosing GPLs and PVDF as the reinforcing fillers and the polymer matrix, respectively, the EMT model on predicting the dielectric permittivity of GPL/PVDF composites was validated by Xia et al. [26].

2.2. Effective elastic modulus

Substituting the parameters with mechanical quantities, Eq. (7) becomes the following form

$$\varphi_{\text{m}} \frac{E_{\text{m}} - E_{\text{e}}}{E_{\text{e}} + (1/3)(E_{\text{m}} - E_{\text{e}})} + \frac{1}{3}\varphi_{\text{f}} \sum_{k=1}^{3} \frac{E_k - E_{\text{e}}}{E_{\text{e}} + S_{kk}(E_k - E_{\text{e}})} = 0 \tag{16}$$

where E_{e} is the elastic modulus of the homogeneous GPLRC. Like the electrical property, considering the imperfect bonding between fillers and polymer, the effective elastic modulus of coated GPL is

$$E_k^{(\text{c})} = E_0^{(\text{int})} \left[1 + \frac{(1-\varphi_{\text{int}})\left(E_k - E_0^{(\text{int})}\right)}{\varphi_{\text{int}} S_{kk}\left(E_k - E_0^{(\text{int})}\right) + E_0^{(\text{int})}} \right] \quad k = 1,2,3 \tag{17}$$

where $E_0^{(\text{int})}$ is the elastic modulus of the interphase. This elastic modulus of coated GPLs will substitute E_k in Eq. (17). Excellent prediction on elastic modulus by EMT model is observed comparing with the experimental data in [53].

3. Problem Formulation

Employing Timoshenko beam theory, the displacement field is given as

$$\begin{cases} \tilde{U}(x,z,t) = U(x,t) - z\Psi(x,t) \\ \tilde{W}(x,z,t) = W(x,t) \end{cases} \tag{18}$$

where $U(x, t)$ and $W(x, t)$ are the displacements of the middle plane of the beam in x and z directions, respectively, $\Psi(x, t)$ is the rotation of the cross section and t is the time. Using von Kármán geometrical nonlinearity, the normal and shear strains in the beam are

$$\begin{cases} \tilde{\varepsilon}_{xx} = \dfrac{\partial \tilde{U}}{\partial x} + \dfrac{1}{2}\left(\dfrac{\partial \tilde{W}}{\partial x}\right)^2 = \dfrac{\partial U}{\partial x} + \dfrac{1}{2}\left(\dfrac{\partial W}{\partial x}\right)^2 - z\dfrac{\partial \Psi}{\partial x} \\ \tilde{\gamma}_{xz} = \dfrac{\partial \tilde{U}}{\partial z} + \dfrac{\partial \tilde{W}}{\partial x} = -\Psi + \dfrac{\partial W}{\partial x} \end{cases} \tag{19}$$

Correspondingly, the normal stress and shear stress are obtained as

$$\begin{cases} \tilde{\sigma}_{xx} = \dfrac{E}{1-\nu^2}\tilde{\varepsilon}_{xx} = \dfrac{E}{1-\nu^2}\left[\dfrac{\partial U}{\partial x} + \dfrac{1}{2}\left(\dfrac{\partial W}{\partial x}\right)^2 - z\dfrac{\partial \Psi}{\partial x}\right] \\ \tilde{\tau}_{xz} = \dfrac{E}{1-\nu^2}\dfrac{1-\nu}{2}\tilde{\gamma}_{xz} = \dfrac{E}{1-\nu^2}\dfrac{1-\nu}{2}\left(-\Psi + \dfrac{\partial W}{\partial x}\right) \end{cases} \tag{20}$$

where E and v represent the elastic modulus and Poisson's ratio of the material of the beam, respectively. Considering an existing axial stress $\tilde{\sigma}$ in the beam, the total normal stress is updated as

$$\tilde{\sigma}_{xx} = \tilde{\sigma} + \frac{E}{1-\nu^2}\left[\frac{\partial U}{\partial x} + \frac{1}{2}\left(\frac{\partial W}{\partial x}\right)^2 - z\frac{\partial \Psi}{\partial x}\right] \tag{21}$$

The existing axial stress in the beam can be determined as following

$$\tilde{\sigma} = \tilde{\sigma}_0 - \varepsilon\frac{V^2}{h^2} \tag{22}$$

where $\tilde{\sigma}_0$ denotes initial stress applied in the beam's longitudinal direction, ε is the dielectric permittivity of the material. V is the voltage applied across the beam. In Eq. (22), the second term on the right hand side denotes the electrostatic stress produced by the voltage due to the dielectric property of the beam. The voltage applied consists of two parts, i.e. $V = V_{DC}+V_{AC}\sin(2\pi f_{AC}t)$, in which V_{DC} and V_{AC} are the amplitudes of DC and AC voltage, respectively, and f_{AC} is the AC frequency of the voltage in Hertz. Here

it should be noted the AC voltage is normally used for actively tuning or periodic excitation and its magnitude is usually much smaller than DC component [54]. Therefore, the magnitude of DC voltage will be used in Eq. (22) to calculate the axial stress.

Integrating the normal and shear stresses over corresponding domains, the internal forces and moment in the beam are derived as

$$\begin{cases} N_x = \int_{-h/2}^{h/2} \tilde{\sigma}_{xx} dz = A_{00}\tilde{\sigma} + A_{11}\left[\dfrac{\partial U}{\partial x} + \dfrac{1}{2}\left(\dfrac{\partial W}{\partial x}\right)^2\right] - B_{11}\dfrac{\partial \Psi}{\partial x} \\ M_x = \int_{-h/2}^{h/2} \tilde{\sigma}_{xx} z dz = B_{00}\tilde{\sigma} + B_{11}\left[\dfrac{\partial U}{\partial x} + \dfrac{1}{2}\left(\dfrac{\partial W}{\partial x}\right)^2\right] - D_{11}\dfrac{\partial \Psi}{\partial x} \\ Q_x = \int_{-h/2}^{h/2} \tilde{\tau}_{xz} dz = A_{55}\left(-\Psi + \dfrac{\partial W}{\partial x}\right) \end{cases} \tag{23}$$

where A_{00}, B_{00}, A_{11}, B_{11}, D_{11} and A_{55} are coefficients determined as

$$\begin{cases} \left\{A_{00}, B_{00}\right\} = \int_{-h/2}^{h/2} \left\{1, z\right\} dz \\ \left\{A_{11}, B_{11}, D_{11}\right\} = \int_{-h/2}^{h/2} E\left\{1, z, z^2\right\} dz \\ \left\{A_{55}\right\} = \int_{-h/2}^{h/2} \dfrac{E}{1-\nu^2}\dfrac{1-\nu}{2} k_s dz \end{cases} \tag{24}$$

with k_s being the shear correction factor.

Based on the stress and strain, the virtual strain energy in the beam can be given as

$$\delta\Pi_S = \int_V \left(\tilde{\sigma}_{xx}\delta\tilde{\varepsilon}_{xx} + \tilde{\tau}_{xz}\delta\tilde{\gamma}_{xz}\right) dV = \int_0^L \left\{ N_x \delta\left[\frac{\partial U}{\partial x} + \frac{1}{2}\left(\frac{\partial W}{\partial x}\right)^2\right] - M_x \delta\frac{\partial \Psi}{\partial x} + Q_x \delta\left(-\Psi + \frac{\partial W}{\partial x}\right)\right\} dx \tag{25}$$

The kinetic energy of the beam is

$$\begin{aligned} \Pi_{\mathrm{T}} &= \frac{1}{2}\int_V \left[\rho\left(\frac{\partial \tilde{U}}{\partial t}\right)^2 + \rho\left(\frac{\partial \tilde{W}}{\partial t}\right)^2 + \rho z^2\left(\frac{\partial \Psi}{\partial t}\right)^2 \right] dV \\ &= \frac{1}{2}\int_0^L \left\{ I_1\left[\left(\frac{\partial U}{\partial t}\right)^2 + \left(\frac{\partial W}{\partial t}\right)^2\right] - 2I_2\left(\frac{\partial U}{\partial t}\right)\left(\frac{\partial \Psi}{\partial t}\right) + 2I_3\left(\frac{\partial \Psi}{\partial t}\right)^2 \right\} dx \end{aligned} \tag{26}$$

where I_1, I_2, I_3 are inertial components defined as

$$\{I_1, I_2, I_3\} = \int_{-h/2}^{h/2} \rho\{1, z, z^2\}\, dz \tag{27}$$

Considering external loading $Q(x, t)$, the virtual work done by this load is

$$\delta W_e = \int_0^L Q(x,t)\,\delta W dx \tag{28}$$

Based on Hamilton's principle, the governing equations for bending and vibration behaviours can be obtained as

$$\int_0^t \left(\delta W_e + \delta T - \delta U\right) dt = 0 \tag{29}$$

Setting the coefficients of δU, δW and $\delta \Psi$ in Eq. (29) as zero produces

$$\begin{cases} \dfrac{\partial N_x}{\partial x} = I_1 \dfrac{\partial^2 U}{\partial t^2} - I_2 \dfrac{\partial^2 \Psi}{\partial t^2} \\ \dfrac{\partial\left(N_x \dfrac{\partial W}{\partial x}\right)}{\partial x} + \dfrac{\partial\left(Q_x\right)}{\partial x} = I_1 \dfrac{\partial^2 W}{\partial t^2} - Q(x,t) \\ \dfrac{\partial M_x}{\partial x} - Q_x = I_2 \dfrac{\partial^2 U}{\partial t^2} - 2I_3 \dfrac{\partial^2 \Psi}{\partial t^2} \end{cases} \tag{30}$$

The governing equations of the beam can be derived by replacing Eq. (23) into Eq. (30) as

$$\begin{cases} A_{11}\left(\dfrac{\partial^2 U}{\partial x^2}+\dfrac{\partial W}{\partial x}\dfrac{\partial^2 W}{\partial x^2}\right)-B_{11}\dfrac{\partial^2 \Psi}{\partial x^2}=I_1\dfrac{\partial^2 U}{\partial t^2}-I_2\dfrac{\partial^2 \Psi}{\partial t^2} \\ A_{00}\tilde{\sigma}\dfrac{\partial^2 W}{\partial x^2}+A_{11}\left[\dfrac{\partial^2 U}{\partial x^2}\dfrac{\partial W}{\partial x}+\dfrac{\partial U}{\partial x}\dfrac{\partial^2 W}{\partial x^2}+\dfrac{3}{2}\left(\dfrac{\partial W}{\partial x}\right)^2\dfrac{\partial^2 W}{\partial x^2}\right] \\ -B_{11}\left(\dfrac{\partial^2 \Psi}{\partial x^2}\dfrac{\partial W}{\partial x}+\dfrac{\partial \Psi}{\partial x}\dfrac{\partial^2 W}{\partial x^2}\right)+A_{55}\left(-\dfrac{\partial \Psi}{\partial x}+\dfrac{\partial^2 W}{\partial x^2}\right)=I_1\dfrac{\partial^2 W}{\partial t^2}-Q(x,t) \\ -B_{11}\left(\dfrac{\partial^2 U}{\partial x^2}+\dfrac{\partial W}{\partial x}\dfrac{\partial^2 W}{\partial x^2}\right)+D_{11}\dfrac{\partial^2 \Psi}{\partial x^2}+A_{55}\left(-\Psi+\dfrac{\partial W}{\partial x}\right)=-I_2\dfrac{\partial^2 U}{\partial t^2}+2I_3\dfrac{\partial^2 \Psi}{\partial t^2} \end{cases} \tag{31}$$

For clamped end (denoted as C), the boundary conditions can be obtained by setting axial and transverse displacements together with rotations as zero, i.e. $U = 0$, $W = 0$ and $\Psi = 0$. Setting the axial and transverse displacements and bending moments as zero will produce the corresponding boundary conditions for hinged end (denoted as H), i.e. $U = 0$, $W = 0$ and $M_x = 0$.

4. Solution

To normalize the governing equations, the following dimensionless quantities are defined

$$\begin{aligned} &\xi=\frac{x}{L},\quad \{u,w\}=\frac{\{U,W\}}{h},\quad \psi=\Psi,\quad \tau=\frac{t}{L}\sqrt{\frac{A_{110}}{I_{10}}},\quad \eta=\frac{L}{h},\quad q=\frac{Q}{A_{110}}\eta L \\ &\{a_{00},a_{11},a_{55},b_{00},b_{11},d_{11}\}=\left\{\frac{A_{00}}{A_{110}},\frac{A_{11}}{A_{110}},\frac{A_{55}}{A_{110}},\frac{B_{00}}{A_{110}h},\frac{B_{11}}{A_{110}h},\frac{D_{11}}{A_{110}h^2}\right\} \\ &\lambda=\omega/\omega_l,\quad \{\bar{I}_1,\bar{I}_2,\bar{I}_3\}=\left\{\frac{I_1}{I_{10}},\frac{I_2}{I_{10}h},\frac{I_3}{I_{10}h^2}\right\} \end{aligned} \tag{32}$$

where A_{110} and I_{10} are the corresponding values of A_{11} and I_1 of beam made of pure polymer, respectively, λ is the dimensionless excitation frequency, and ω and ω_l are the radian excitation frequency and corresponding fundamental frequency of the composites beam, respectively. Then Eq. (31) can be cast as the following dimensionless form

$$\begin{cases} a_{11}\left(\dfrac{\partial^2 u}{\partial \xi^2}+\dfrac{1}{\eta}\dfrac{\partial w}{\partial \xi}\dfrac{\partial^2 w}{\partial \xi^2}\right)-b_{11}\dfrac{\partial^2 \psi}{\partial \xi^2}=\bar{I}_1\dfrac{\partial^2 u}{\partial \tau^2}-\bar{I}_2\dfrac{\partial^2 \psi}{\partial \tau^2} \\ a_{00}\tilde{\sigma}\dfrac{\partial^2 w}{\partial \xi^2}+a_{11}\left[\dfrac{1}{\eta}\dfrac{\partial^2 u}{\partial \xi^2}\dfrac{\partial w}{\partial \xi}+\dfrac{1}{\eta}\dfrac{\partial u}{\partial \xi}\dfrac{\partial^2 w}{\partial \xi^2}+\dfrac{3}{2}\dfrac{1}{\eta^2}\left(\dfrac{\partial w}{\partial \xi}\right)^2\dfrac{\partial^2 w}{\partial \xi^2}\right] \\ -b_{11}\left(\dfrac{1}{\eta}\dfrac{\partial^2 \psi}{\partial \xi^2}\dfrac{\partial w}{\partial \xi}+\dfrac{1}{\eta}\dfrac{\partial \psi}{\partial \xi}\dfrac{\partial^2 w}{\partial \xi^2}\right)+a_{55}\left(-\eta\dfrac{\partial \psi}{\partial \xi}+\dfrac{\partial^2 w}{\partial \xi^2}\right)=\bar{I}_1\dfrac{\partial^2 w}{\partial \tau^2}-q(\xi,\tau) \\ -b_{11}\left(\dfrac{\partial^2 u}{\partial \xi^2}+\dfrac{1}{\eta}\dfrac{\partial w}{\partial \xi}\dfrac{\partial^2 w}{\partial \xi^2}\right)+d_{11}\dfrac{\partial^2 \psi}{\partial \xi^2}+a_{55}\left(-\eta^2\psi+\eta\dfrac{\partial w}{\partial \xi}\right)=-\bar{I}_2\dfrac{\partial^2 u}{\partial \tau^2}+2\bar{I}_3\dfrac{\partial^2 \psi}{\partial \tau^2} \end{cases} \tag{33}$$

The dimensionless governing equations can be solved numerically with the aid of differential quadrature method (DQM). First, the following forms for displacements of the beam and their derivatives are introduced

$$\begin{cases} \{u,w,\psi\}=\sum_{m=1}^{N} l_m(x)\{u_m,w_m,\psi_m\} \\ \dfrac{\partial^k}{\partial \xi^k}\{u,w,\psi\}\Big|_{\xi=\xi_i}=\sum_{m=1}^{N} c_{im}^{(k)}\{u_m,w_m,\psi_m\} \end{cases} \tag{34}$$

where $\{u_m,w_m,\psi_m\}$ is the displacement vector at position $\xi = \xi_{\mathrm{m}}$, $l_m(x)$ is the Lagrange interpolation polynomials and $c_{im}^{(k)}$ is the weighting coefficients of the kth derivative at $\xi = \xi_i$, and N is the total number of grid points distributed along the whole length of the beam. In present work, we adopted the following expression for the distribution of the grid points [55]

$$\xi_i=\frac{1}{2}\left[1-\cos\frac{\pi(i-1)}{N-1}\right]\ (i=1,2,\cdots,N) \tag{35}$$

Substituting Eq. (34) into Eq. (33) will yield the governing equations in the following discretized form

$$\begin{cases} a_{11}\left(\sum_{m=1}^{N}c_{im}^{(2)}u_m+\frac{1}{\eta}\sum_{m=1}^{N}c_{im}^{(1)}w_m\sum_{m=1}^{N}c_{im}^{(2)}w_m\right)-b_{11}\sum_{m=1}^{N}c_{im}^{(2)}\psi_m=\bar{I}_1\ddot{u}_i-\bar{I}_2\ddot{\psi}_i \\ a_{00}\tilde{\sigma}\sum_{m=1}^{N}c_{im}^{(2)}w_m+a_{11}\left[\frac{1}{\eta}\sum_{m=1}^{N}c_{im}^{(2)}u_m\sum_{m=1}^{N}c_{im}^{(1)}w_m+\frac{1}{\eta}\sum_{m=1}^{N}c_{im}^{(1)}u_m\sum_{m=1}^{N}c_{im}^{(2)}w_m+\frac{3}{2}\frac{1}{\eta^2}\left(\sum_{m=1}^{N}c_{im}^{(1)}w_m\right)^2\sum_{m=1}^{N}c_{im}^{(2)}w_m\right] \\ -b_{11}\left(\frac{1}{\eta}\sum_{m=1}^{N}c_{im}^{(2)}\psi_m\sum_{m=1}^{N}c_{im}^{(1)}w_m+\frac{1}{\eta}\sum_{m=1}^{N}c_{im}^{(1)}\psi_m\sum_{m=1}^{N}c_{im}^{(2)}w_m\right)+a_{55}\left(-\eta\sum_{m=1}^{N}c_{im}^{(1)}\psi_m+\sum_{m=1}^{N}c_{im}^{(2)}w_m\right)=\bar{I}_1\ddot{w}_i-q\left(\xi_i,\tau\right) \\ -b_{11}\left(\sum_{m=1}^{N}c_{im}^{(2)}u_m+\frac{1}{\eta}\sum_{m=1}^{N}c_{im}^{(1)}w_m\sum_{m=1}^{N}c_{im}^{(2)}w_m\right)+d_{11}\sum_{m=1}^{N}c_{im}^{(2)}\psi_m+a_{55}\left(-\eta^2\psi_i+\eta\sum_{m=1}^{N}c_{im}^{(1)}w_m\right)=-\bar{I}_2\ddot{u}_i+2\bar{I}_3\ddot{\psi}_i \end{cases} \tag{36}$$

Correspondingly, the boundary conditions for clamped and hinged ends become

$$u=0,\ w=0,\ \psi=0 \tag{37}$$

and

$$u=0,\ w=0,\ b_{00}\eta+b_{11}\left[\sum_{m=1}^{N}c_{im}^{(1)}u_m+\frac{1}{2\eta}\left(\sum_{m=1}^{N}c_{im}^{(1)}w_m\right)^2\right]-d_{11}\sum_{m=1}^{N}c_{im}^{(1)}\psi_m=0 \tag{38}$$

Eq. (36) can also be re-arranged in a simplified matrix form as

$$\boldsymbol{M}\ddot{\boldsymbol{d}}+\left[\boldsymbol{K}_{\mathrm{L}}+\boldsymbol{K}_{\mathrm{NL}}\left(\boldsymbol{d}\right)\right]\boldsymbol{d}=\boldsymbol{q} \tag{39}$$

where $\boldsymbol{K}_{\mathrm{L}}$ denotes linear stiffness matrix, $\boldsymbol{K}_{\mathrm{NL}}$ denotes the nonlinear stiffness matrix depending on displacement vector $\boldsymbol{d}=\left\{\left\{u_i\right\}^T,\left\{w_i\right\}^T,\left\{\psi_i\right\}^T\right\}^T$, $\boldsymbol{M}$ denotes mass matrix and $\boldsymbol{q}$ denotes force vector expressed as

$$\boldsymbol{q}=\left\{\left\{0\right\}_{N\times1}^T,\left\{q\left(\xi_i,\tau\right)\right\}_{N\times1}^T,\left\{0\right\}_{N\times1}^T\right\}^T\quad\left(i=1,2,\cdots,N\right) \tag{40}$$

Considering damping of the system, Eq. (39) can also be written as

$$\boldsymbol{M}\ddot{\boldsymbol{d}} + \boldsymbol{C}\dot{\boldsymbol{d}} + \left(\boldsymbol{K}_{\mathrm{L}} + \boldsymbol{K}_{\mathrm{NL}}\right)\boldsymbol{d} = \boldsymbol{q} \tag{41}$$

where $\boldsymbol{C} = (2\zeta/\omega_l)/\boldsymbol{K}_{\mathrm{L}}$ is the damping coefficient matrix defined with ζ being damping ratio and ω_l the beam's fundamental natural frequency [56]. For nonlinear bending of the composite beam, Eq. (41) can be reduced to

$$\left(\boldsymbol{K}_{\mathrm{L}} + \boldsymbol{K}_{\mathrm{NL}}\right)\boldsymbol{d} = \boldsymbol{q} \tag{42}$$

where $\boldsymbol{q} = \left\{\{0\}_{N\times 1}^{T}, \{q(\xi_i)\}_{N\times 1}^{T}, \{0\}_{N\times 1}^{T}\right\}^{T}$ $(i = 1, 2, \cdots, N)$.

Eq. (42) can be solved by direct iteration method for nonlinear bending while the time response of the beam under transverse load can be obtained through solving Eq. (41) with direction integration by Runge-Kutta method.

5. Results and Discussion

5.1. Convergence and Validation Study

Table 1 tabulates dimensionless midpoint deflection of GPL/PVDF composite beams with different numbers of grid points and boundary conditions. The concentration of GPL in the composites is 1.5 wt%. The dimensions of the beam are L = 10 mm and h = 0.5 mm, respectively. No electrical field and initial axial stress and are applied on the beam. The total number of grid points N increases from 7 to 25. As can be seen, grid points are required to achieve convergent results for beams subjected to larger loading. For example, 17 grid points are needed to achieve convergent results for H-H beam when the dimensionless load is 0.01 while 23 grid points are required as the dimensionless load increases to 0.03. Considering computational efficiency with enough accuracy, 19 grid points will be used for analysis thereafter.

Table 1 Dimensionless midpoint deflection of GPLRC beam with different boundary conditions.

N	q = 0.01			q = 0.03		
	C-C	C-H	H-H	C-C	C-H	H-H
7	0.049122	0.095589	0.210426	0.145767	0.262646	0.483511
9	0.049103	0.095574	0.210428	0.145293	0.262355	0.465535
11	0.049103	0.095574	0.210428	0.145293	0.262357	0.465868

13	0.049103	0.095574	0.210428	0.145293	0.262357	0.46599
15	0.049103	0.095574	0.210428	0.145293	0.262357	0.465978
17	0.049103	0.095574	0.210428	0.145293	0.262357	0.465978
19	0.049103	0.095574	0.210428	0.145293	0.262357	0.465978
21	0.049103	0.095574	0.210428	0.145293	0.262357	0.465978
23	0.049103	0.095574	0.210428	0.145293	0.262357	0.465978
25	0.049103	0.095574	0.210428	0.145293	0.262357	0.465978

The numerical results are validated by comparing the dimensionless midpoint deflections of a C-C isotropic homogenous beam with the results by Feng et al. [29] and Reddy et al. [57] in Table 2. The elastic modulus and Poisson's ratio are $E = 30\times10^6$ psi and $v = 0.3$, respectively. The dimensions of the beam are $b = h = 1$ in and $L = 100$ in. The comparison indicates the present results agree well with FEM and previous reported results, especially for bigger external loadings.

Table 2 Comparion of dimensionless midpoint deflections of beams with various loadings.

Q (lb/in)	Centre deflection (in)			
	Present	FEM	Feng et al. [29]	Reddy et al. [57]
1	0.10349	0.10349	0.09853	0.10271
5	0.45339	0.45354	0.44972	0.45003
10	0.74344	0.74380	0.72753	0.74132

5.2. Nonlinear Bending

As indicated, the beam thickness will have obvious effect on the beam's axial stress. In this sub-section, an H-H GPL/PVDF beam will be considered for parametric study on nonlinear bending. Fig. 2 examines the effects of the beam thickness on the dimensionless midpoint deflection of the beam. As expected, with the increase of the beam thickness, the deflection decreases due to the change in the beam geometry. The effects of beam thickness on the deflection depend on the applied electrical voltage, especially when the beam thickness is relatively small. With the same beam thickness, the deflection enhances as the electrical voltage increases. For example, as the beam thickness increases from 0.5 mm to 1.0 mm, the deflections decrease by 53.40% and 68.70% when the voltage is 0 V and 250 V, respectively. However, as the beam

thickness becomes sufficiently large, the electrical voltage will have limited effects on the deflection. The above phenomena can be explained by the fact that when the beam thickness is relatively small, the reduction in the axial stress of beam due to electrical voltage is very significant, resulting in significant drop in the rigidity of the beam. As the beam thickness increases to sufficiently large, the variation of axial stress in the beam due to electrical voltage become limited, resulting in the overlap of the curves regardless of the magnitude of the voltage. The above analysis suggests that with fixed beam geometry, the bending behaviours of the beam can be actively tuned by changing applied electrical voltage.

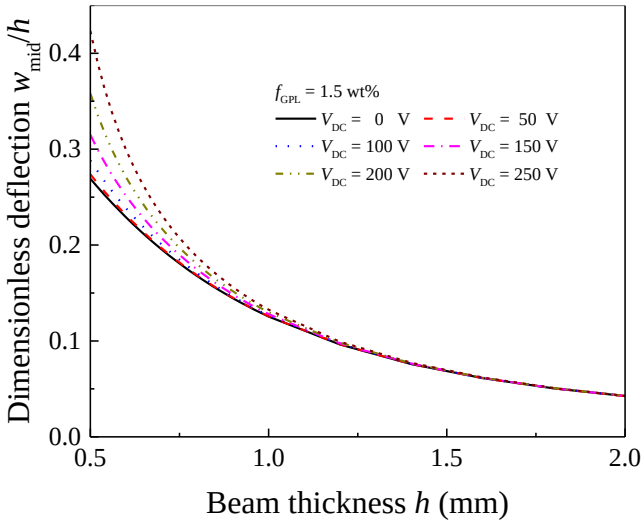

Fig. 2. Variation of dimensionless midpoint deflection with thickness of GPL/PVDF beam.

Fig. 3 plots the variation of the dimensionless midpoint deflection of the GPL/PVDF beam. As seen from Fig. 3a, the same decrease of the dimensionless midpoint deflection is observed when GPL concentration reaches a critical value, i.e. f_{GPL} = 1.3 wt%, for all voltages considered. However, when GPL concentration further increases, the deflection becomes highly dependent on the applied electrical voltage. For example, when the applied voltage is 0 V, the deflection undergoes a minor decrease from 0.28084 to 0.24293 when the GPL weight fraction increases from 1.3 wt% to 2 wt%. As the voltage increases, the deflection of the beam diverges depending on the magnitude of the voltage. Particularly, the deflection even starts to increase for higher voltages. For example, when the applied voltage reaches 50 V, the dimensionless deflection grows from 0.28084 to 0.29702 as the GPL weight fraction increases from 1.3 wt% to 2 wt%. These results are owning to the fact that when the GPL concentration is below the percolation threshold, the variation of the beam deflection is ascribed to the change of the elastic modulus

of the composites. Once the GPL concentration exceeds its percolation threshold, the electrical voltage will significantly reduce the axial stress, resulting in increase of the beam deflection. In Fig. 3b, the magnitude of DC voltage is fixed as 50 V while the AC frequency varies from 0 Hz and 10^7 Hz. Similar trend of the dependency of the deflection on GPL weight fraction is found as observed in Fig. 3a. A snap-through phenomenon is observed for the bending deflection of the beam when the GPL concentration exceeds the critical GPL concentration. When AC frequency is less than 10 Hz the curves converge to constitute the upper limit of the deflection. The deflection drops dramatically to a position when the AC frequency increases to 100. Then curves converge once again and constitute the lower limit of deflection when the AC frequency becomes greater than 10^3 Hz. This indicates that the bending deflection of the beam is very sensitive to a certain range of AC frequency (i.e. around 100 Hz in this case).

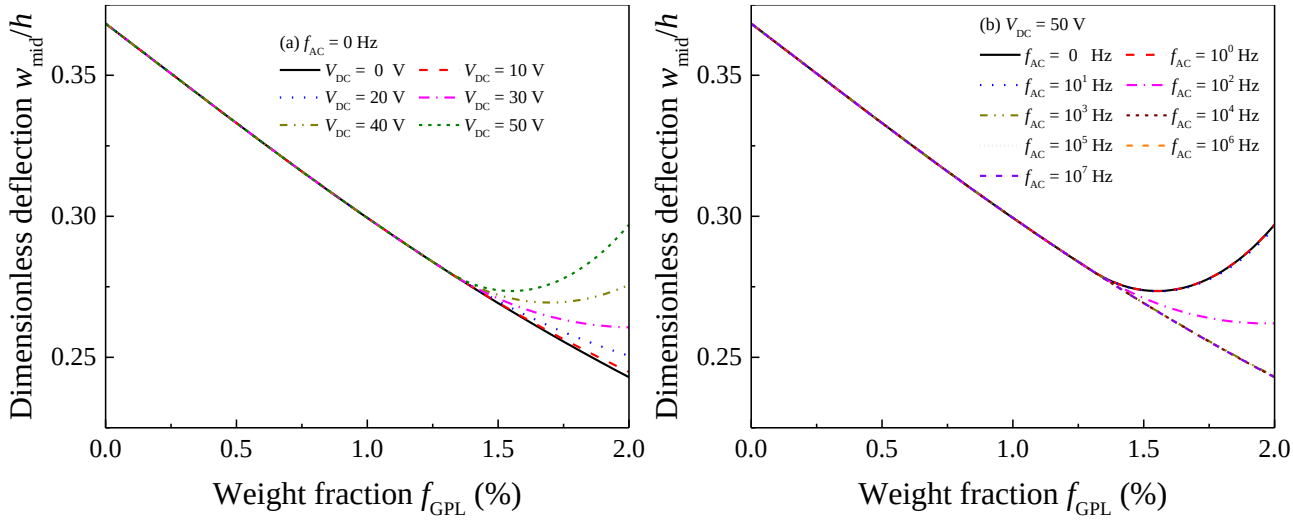

Fig. 3. Variation of dimensionless deflection of GPL/PVDF beam with GPL concentration (a) f_{AC} = 0 Hz; (b) V_{DC} = 50 V.

Fig. 4 demonstrates the dependency of dimensionless midpoint deflection of GPL/PVDF beam on the GPL aspect ratio D_{GPL}/t_{GPL}, in which the GPL thickness is fixed as 50 nm. The GPL concentration in this case is 1.5 wt%. As seen from the figure, the dimensionless deflections for different AC frequency overlap each other for all voltages considered, i.e. 10 V, 20 V, 30 V and 40 V, when the GPL aspect ratio is a critical value, i.e. approximate 200. As the GPL aspect ratio further increases, i.e. larger than 200, AC frequency demonstrates different influences on the deflection for different electrical voltages. For example, the deflection always drops with the GPL aspect ratio for relatively low voltages, i.e. 10 V and 20 V, as

demonstrated in Fig. 4a and Fig. 4b. When the electrical voltage increases to larger values, i.e. 30 V and 40 V, as shown in Fig. 4c and Fig. 4d, the deflection of the beam still decreases with the GPL aspect ratio for bigger AC frequency, i.e. 10^3 Hz and 10^4 Hz. However, the deflection starts to increase with the GPL aspect ratio for smaller AC frequency, i.e. 0, 1 and 10 Hz. The above observations can be ascribed to the dependency of the elastic modulus and dielectric permittivity of the composites on the GPL aspect ratio and AC frequency. GPLs with larger aspect ratio can better reinforce the elastic modulus and dielectric permittivity of the nanocomposites. When the GPL aspect ratio is small, i.e. less than 200, the GPL weight fraction is below the percolation threshold and the dielectric property of the composites can be neglected regardless of the magnitudes of the AC frequency and electrical voltages. Thus, the deflection decreases with GPL aspect ratio for all cases owning to increased elastic modulus of the composites. When the GPL aspect ratio increases, the GPL concentration approaches the percolation threshold. For smaller voltage, the decrease of deflection is dominated by the increased elastic modulus. In contrast, for smaller AC frequency at larger electrical voltage, deflection decreased due to dielectric property of the beam becomes more significant compared to the contribution by elastic modulus.

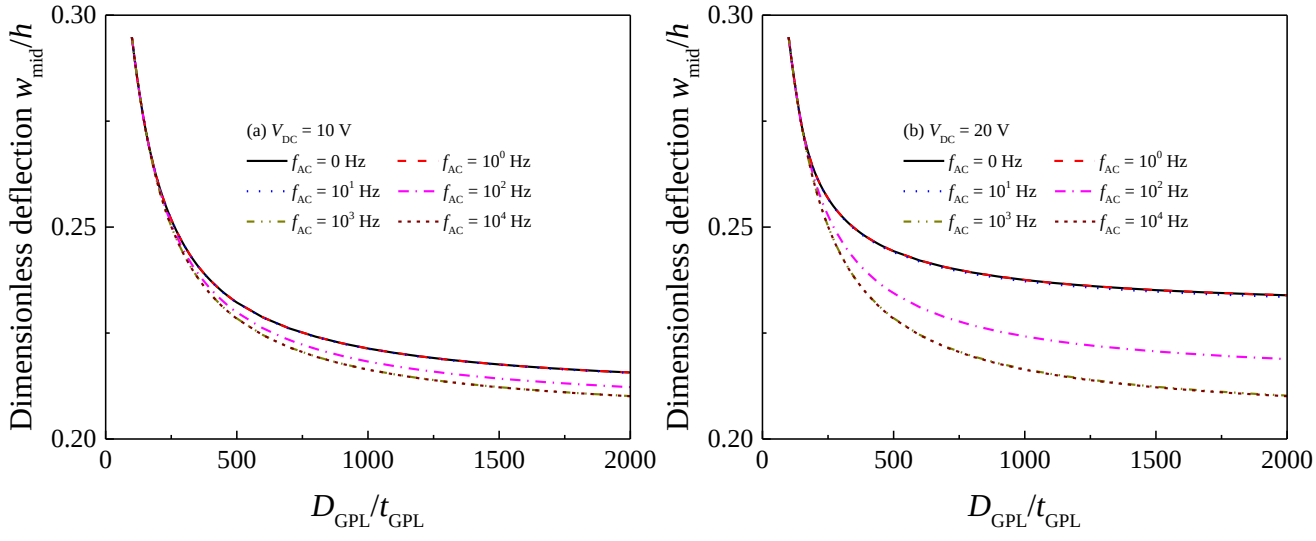

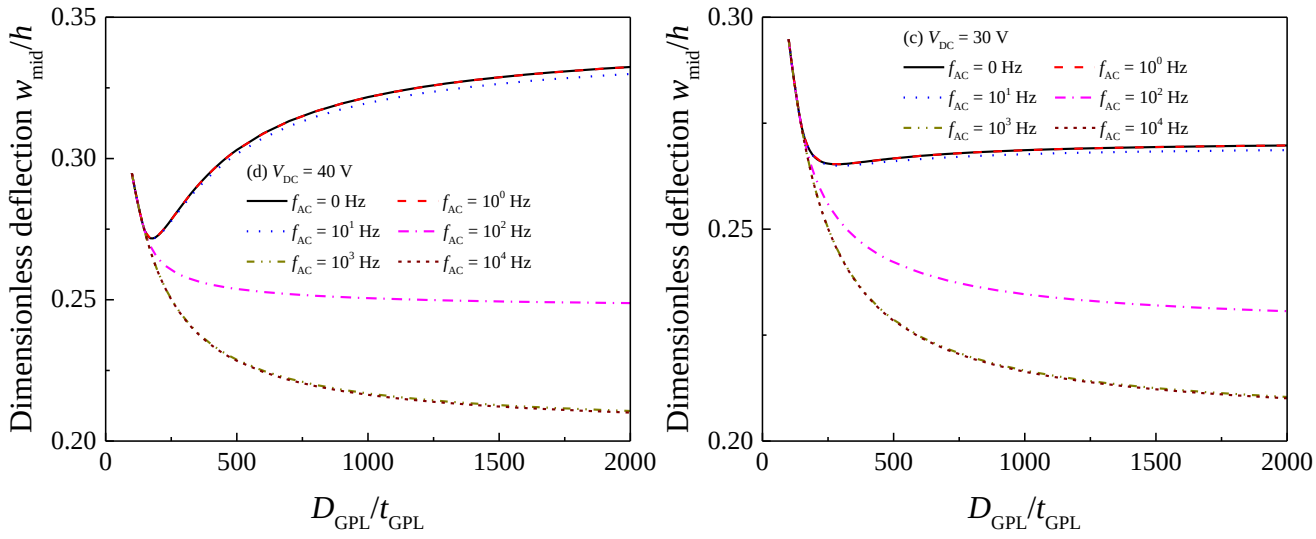

Fig. 4. Variation of dimensionless midpoint deflection of GPL/PVDF with GPL aspect ratio (a) V_{DC} = 10 V (b) V_{DC} = 20 V (c) V_{DC} = 30 V (d) V_{DC} = 40 V.

Fig. 5 plots the variation of the dimensionless midpoint deflection of GPL/PVDF beam with electrical voltage. When the GPL weight fraction is 1.3 wt%, the dimensionless deflection is independent on the electrical voltage. This is because this weight fraction is smaller than the percolation threshold and the dielectric property of the composites and resultant variation in the axial stress can be neglected. As the GPL concentration increases, the deflection increases with enhanced increasing rate. For example, the dimensionless deflection slightly grows from 0.27166 to 0.27657 as the voltage increases from 0 V to 100 V when the GPL concentration is 1.4 wt%. In contrast, the dimensionless deflection goes up from 0.2595 to 0.30665 when the GPL concentration is 1.6 wt%. The above phenomenon is contrary to the trend as normally expected, i.e. the increase of GPL concentration would decrease the deflection due to enhanced beam stiffness. This is because the increase of GPL results in significant enhancement in dielectric property of the composite, softening the stiffness of the beam. Such softening effect is more significant than the increase of beam stiffness due to increased GPL concentration.

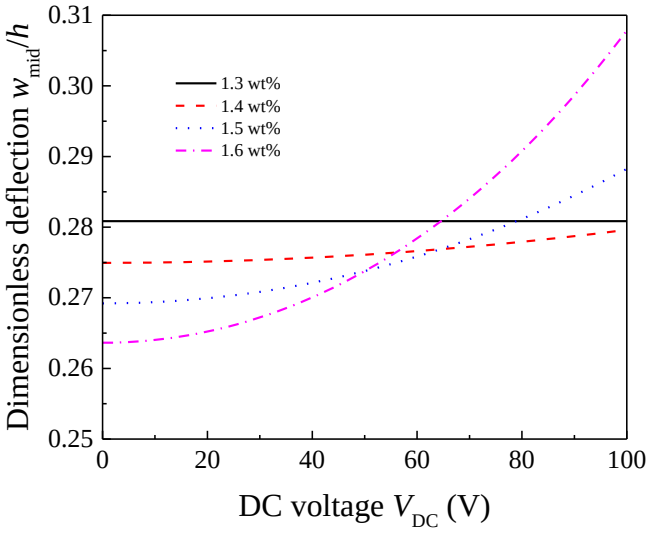

Fig. 5. Variation of dimensionless midpoint deflection of GPL/PVDF composite beam with voltage.

The variation of the dimensionless midpoint deflection of the GPL/PVDF beam with AC frequency is described in Fig. 6. The amplitude of the DC component is fixed as 100 V. As seen from this figure, the dimensionless deflection is independent on the AC frequency when the GPL concentration is relatively low (i.e. f_{GPL} = 1.3 wt%). When the GPL concentration further increases, there exists a transition region, wherein dimensionless deflection decreases sharply as the AC frequency increases. Within the transition region, the increase of the GPL concentration will result in the increase of the variation rate of the dimensionless deflection. As the AC frequency becomes sufficiently large, the dimensionless deflection once again becomes independent on the AC frequency.

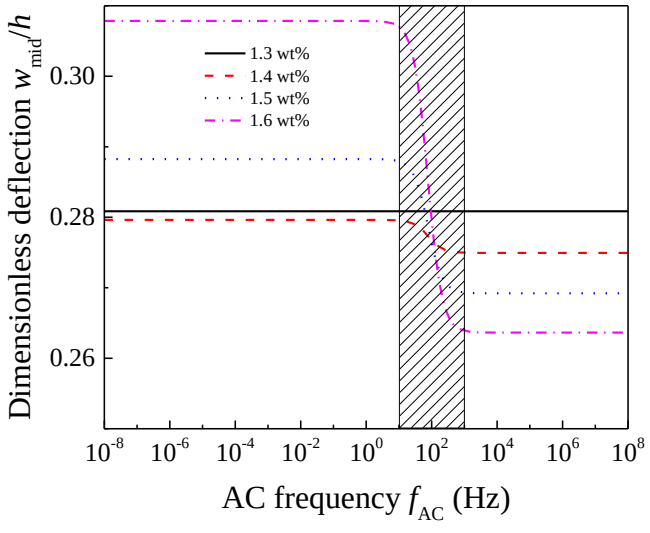

Fig. 6. Variation of dimensionless midpoint deflection of GPL/PVDF composite beam with AC frequency.

5.3. Forced vibration

For forced vibration, steady-state response is of the most interest in engineering practice. Thus, parametric study will be conducted on the steady-state response of C-C composite beams in the following. Unless stated otherwise, the dimensionless amplitude and excitation frequency of the periodic transverse loading are set to be constants, i.e. $q_{max} = 10$ and $\lambda = 5$, respectively, and the damping ratio is $\zeta = 0.1$. Fig. 7 studies the steady-state response of the beam with different thicknesses, in which two voltages, i.e. 0 V and 250 V, are considered. It can be concluded from the figure the vibration amplitude decreases with the increase of the beam thickness owning to enhanced rigidity of the beam. Considering electrical voltage, the vibration amplitude and velocity are more sensitive to the beam with smaller thickness. This can be evidenced by the significant enlargement of the phase portrait for 0.5 mm thickness while the others have limited change when an electrical voltage of 250 V is applied. The significant enlargement of the phase portrait indicates that the beams with smaller thickness will have wider range of reaction when subjected to external loading. This is beneficial for developing smart structures with better capability of active tuning. However, the beam with larger area of phase portrait corresponds to higher energy, which may increase the risk of mechanical failure.

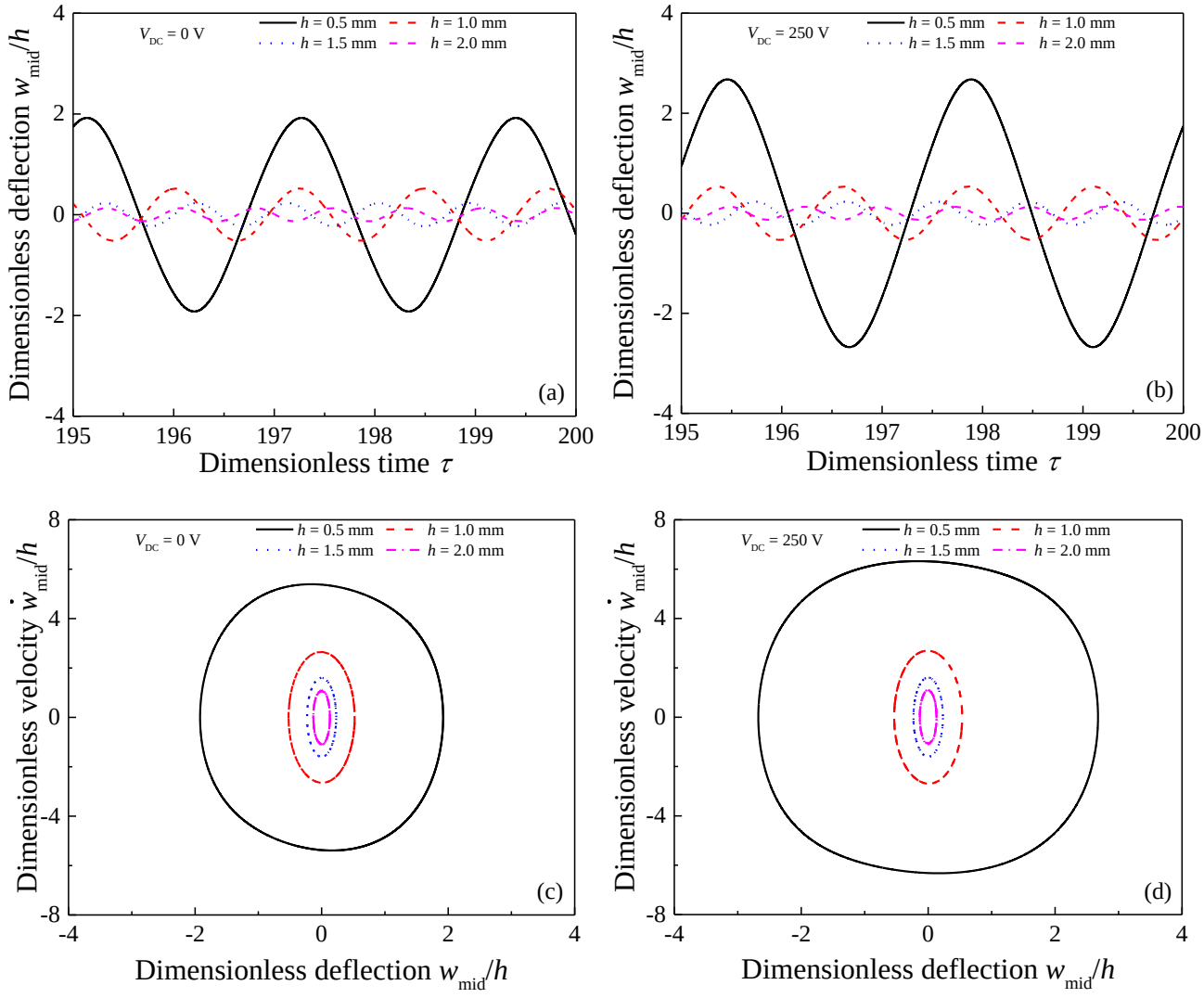

Fig. 7. Steady-state response of GPL/PVDF composite beam with different beam thicknesses (a) Time history at V_{DC} = 0 V; (b) Time history at V_{DC} = 250V; (c) Phase portrait at V_{DC} = 0 V; (b) Phase portrait at V_{DC} = 250 V.

Fig. 8 compares the steady-state responses of GPL/PVDF beam with different initial axial stresses, in which the electrical voltage is set as zero. As observed in Fig. 8a, the vibration amplitude drops with the increase of the initial axial stress due to beam's reinforced stiffness. Shown in Fig. 8b, the phase portrait with initial stress being 2.5 MPa has the largest area, which corresponds to the highest energy in the beam structure. Fig. 9 exhibits the steady-state response of the GPL/PVDF composite beam subjected to different damping ratios, in which the initial axial stress is 10 MPa and no electrical voltage is applied. Expectedly, the vibration amplitude weakens with the increase of the damping ratio. It is found that the

effect of the damping ratio becomes limited as it increases to larger values. Due to the more energy dissipated, the phase portrait shrinks for larger damping ratio as observed in Fig. 9b.

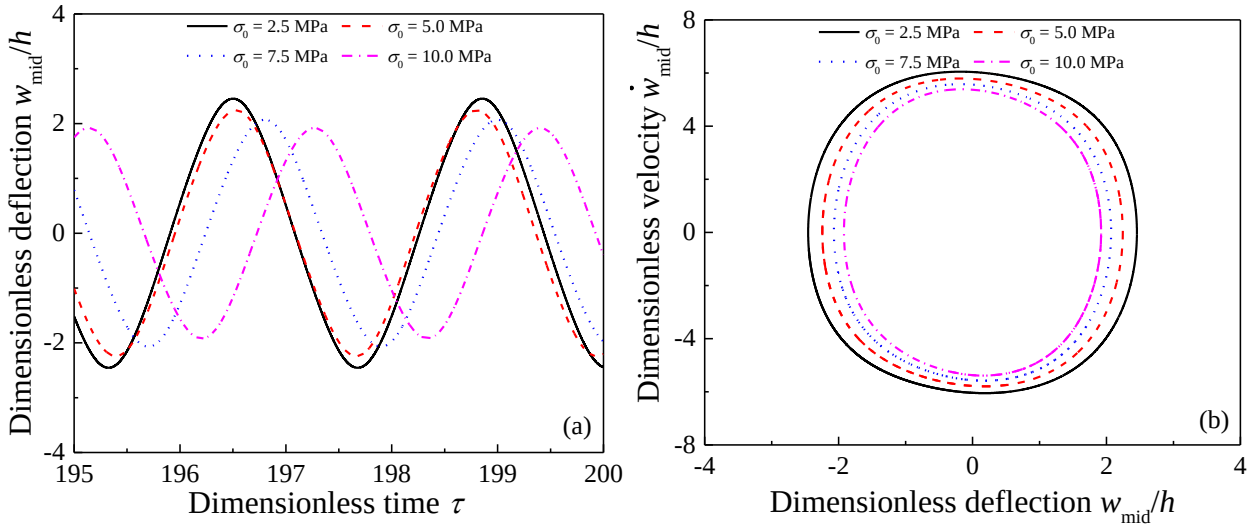

Fig. 8. Steady-state response of GPL/PVDF beam with different initial axial stresses (a) Time history; (b) Phase portrait.

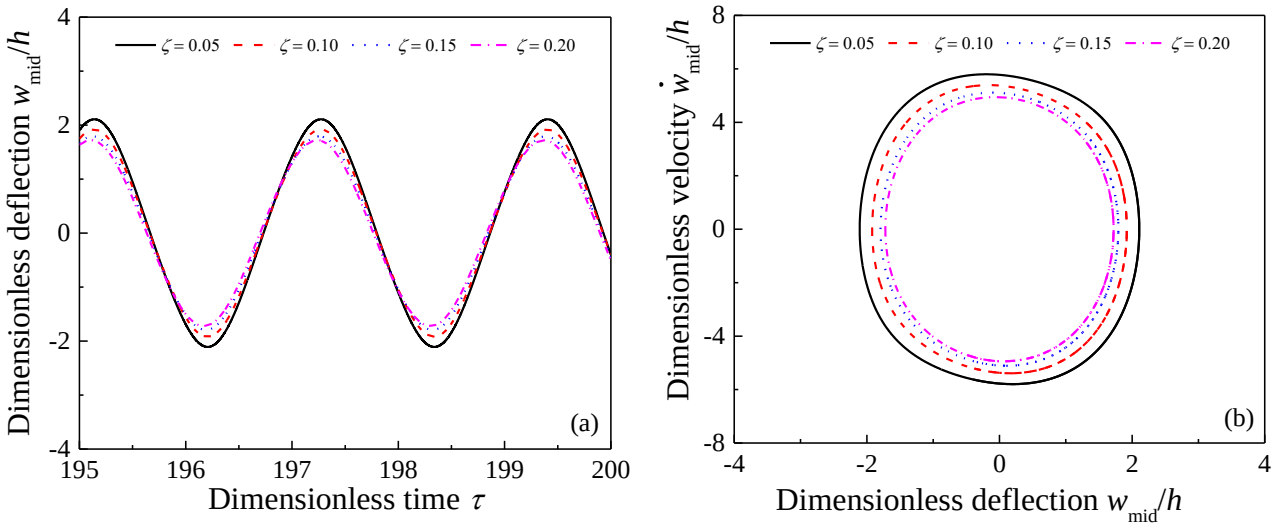

Fig. 9. Steady-state response of GL/PVDF beam with different damping ratios (a) Time history; (b) Phase portrait.

The effects of GPL concentration on the steady-state response of the beam are demonstrated in Fig. 10. Without considering electrical field, the vibration amplitude slightly decreases with the GPL concentration

as demonstrated in Fig. 10a. In contrast, when an electrical voltage of 250 V is applied, the vibration amplitude firstly decreases and then increases as GPL concentration grows (as shown in Fig. 10b). The above observations can also be evidenced by the corresponding phase portraits. For example, without electrical voltage, phase portraits are distributed closely with limited gaps between neighboring ellipses and their area always decreases as the GPL concentration increases (Fig. 10c). This trend is also true for relatively small GPL weight fraction, i.e. 1.2 wt% and 1.3 wt%, when subjected to electrical voltage (Fig. 10d). However, as the GPL further increases, the phase portrait starts to enlarge, which becomes more significant for higher GPL concentration. This non-monotonic variation with GPL concentration with considering electrical voltage is ascribed to the combined effects of electrical voltage and GPL's reinforcement on elastic modulus. The addition of more GPLs enhances the elastic modulus of the composites whereas it decreases the beam's stiffness when considering electrical voltage due to increased dielectric permittivity and resultant release of axial stress. When GPL concentration is small, the increase in beam stiffness by the variation of elastic modulus is more significant than the reduced axial stress by the electrical voltage due to limited dielectric permittivity. As GPL concentration further increases, the significant increase of the dielectric permittivity will release more axial stress, resulting in dominant decrease in the stiffness of the beam.

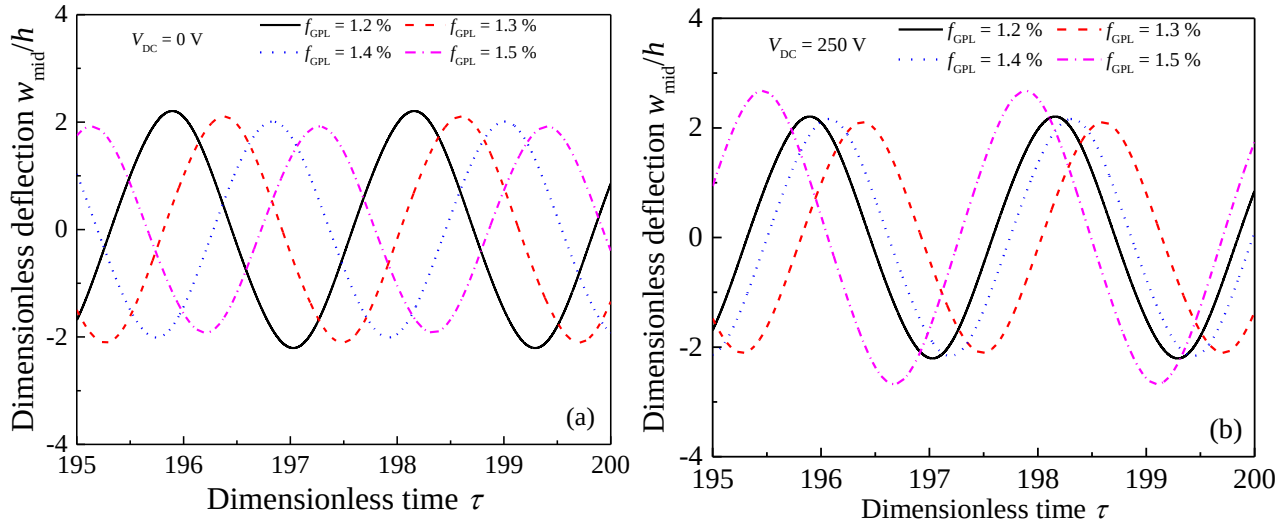

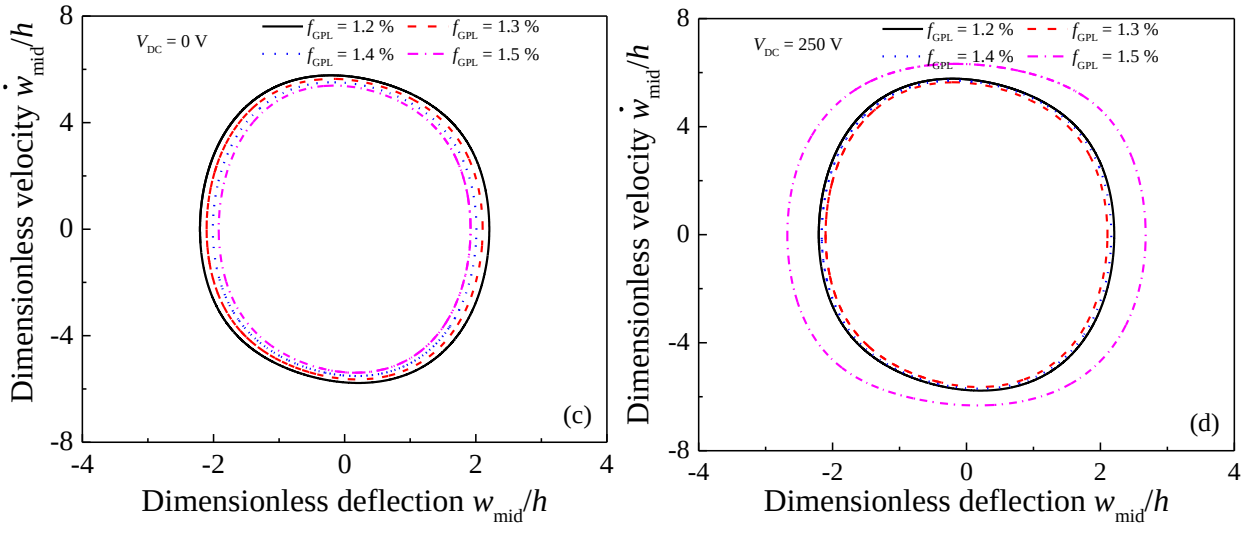

Fig. 10. Steady-state response of GPL/PVDF beam with different GPL weight fractions (a) Time history at V_{DC} = 0; (b) Time history at V_{DC} = 250 V; (c) Phase portrait at V_{DC} = 0 (d) Phase portrait at V_{DC} = 250 V.

The steady-state responses of the composite beam reinforced by GPLs with different aspect ratio are presented in Fig. 11, in which the electrical loading only consists of DC component and two DC voltages, 0 and 100 V are considered. Without applying electrical voltage, i.e. V_{DC} = 0, the vibration amplitude always decreases as the GPL aspect ratio increases. In contrast, when an electrical voltage of 100 V is applied, the GPL aspect ratio has different effects on the vibration amplitude. Seen from Fig. 11b, the vibration amplitudes are almost the same as the ones in Fig. 11a for relatively small GPL aspect ratio, i.e. D_{GPL}/t_{GPL} = 100 and 200. However, as the GPL aspect ratio increases to 300 and 400, the vibration amplitude in Fig. 11b increases instead of decreasing compared to the variation in Fig. 11a. The phase portraits for different voltages also indicate the same trend. For example, in Fig. 11c the area of the elliptical phase portrait decreases steadily as the GPL aspect ratio increases. However, considering the electrical voltage, the elliptical phase portrait enlarges for larger GPL aspect ratios, i.e. D_{GPL}/t_{GPL} = 300 and 400. Particularly, the enlarged phase portraits have some collapses in certain positions. This is attributed to the effects of nonlinear geometry when subjected to large amplitude vibration.

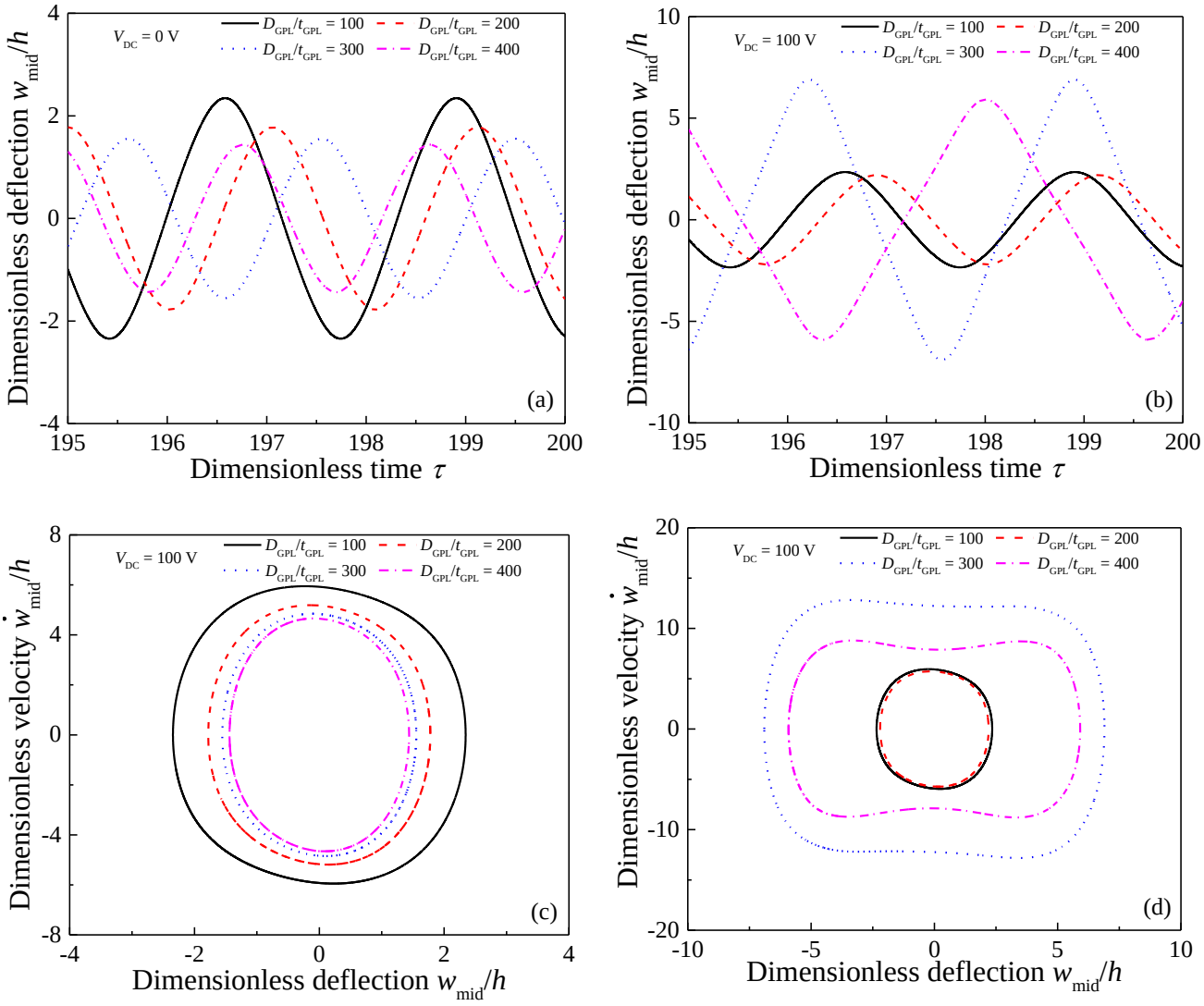

Fig. 11. Steady-state response of GPL/PVDF composite beam with different GPL aspect ratios (a) Time history at V_{DC} = 0; (b) Time history at V_{DC} = 100 V; (c) Phase portrait at V_{DC} = 0; (d) Phase portrait at V_{DC} = 100 V.

The steady-state responses of GPL/PVDF composite beam subjected to different electrical loadings are investigated in Fig. 12, in which the initial axial stress is 10 MPa and AC frequency is set as zero. Seen from Fig. 12a. The increase of the electrical voltage induces larger vibration amplitude as the beam is more softened by the drop in the axial stress. Moreover, it is found that the reaction of the beam to the same external loading is more sensitive for higher electrical voltage. This indicates that applying larger electrical voltage enables the structure to have better actuation performance, which is desired for smart

structures. However, higher voltage should be constrained within a safe range to avoid electrical breakdown of the composites.

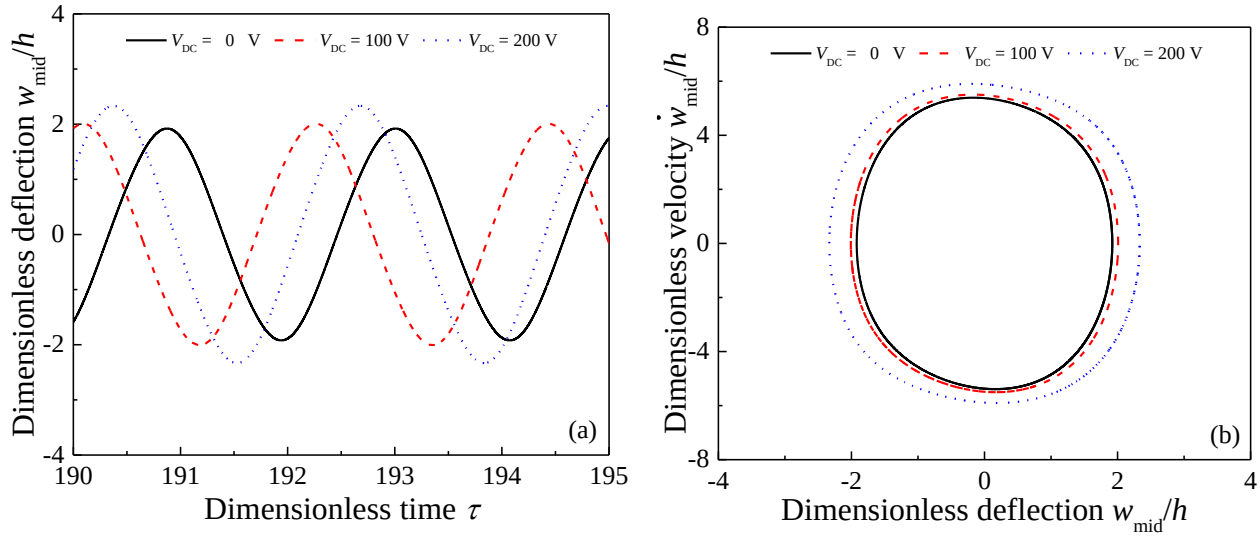

Fig. 12. Steady-state response of GPL/PVDF beam subjected to different electrical voltages (a) Time history; (b) Phase portrait.

Subjected to an electrical voltage of 250 V, the effects of AC frequency on the steady-state response of the beam are presented in Fig. 13. From the time history and the phase portrait, it can be seen that there exists a snap through phenomenon similar to the one for nonlinear bending behaviours. For example, when the AC frequency is small, i.e. 0 and 10 Hz, it has limited effects on the beam's steady-state response of the beam. When the AC frequency reaches 100 Hz, the amplitudes of deflection and velocity jump to certain values. Then the response of the beam converges again as the AC frequency becomes sufficiently large. This snap-through phenomenon is attributed to the dependency of the dielectric permittivity of the composite on the AC frequency, for which there exists a transition region. Within this transition region, the dielectric permittivity drops sharply as the AC frequency increases. Beyond this transition, the dielectric permittivity hardly depends on the AC frequency.

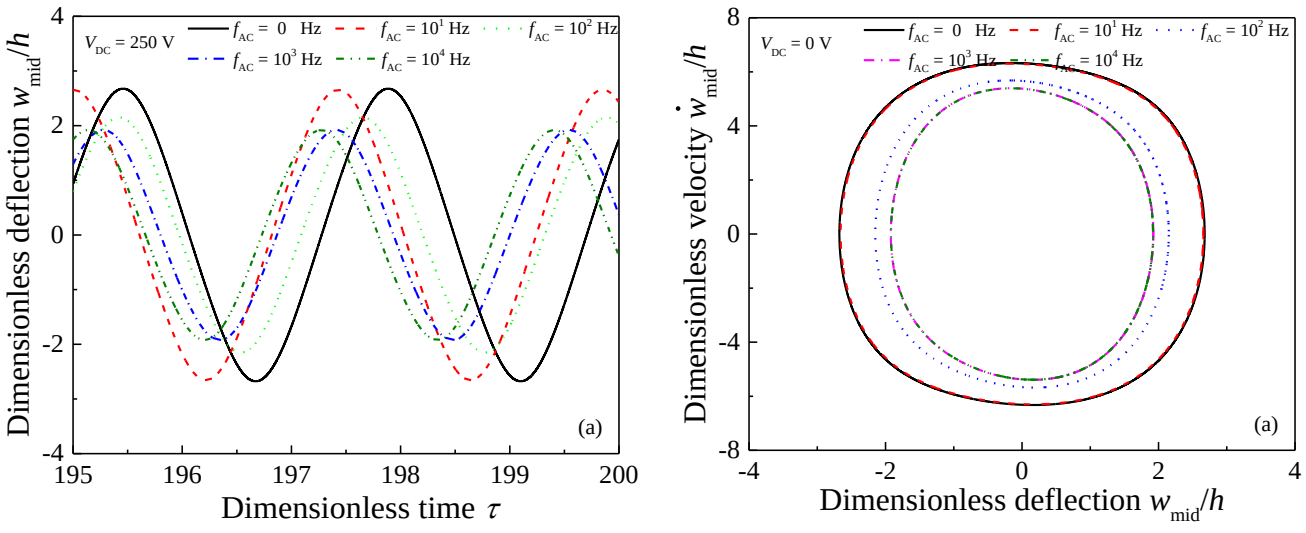

Fig. 13. Steady-state response of GPL/PVDF beam subjected to different AC frequencies (a) Time history; (b) Phase portrait.

6. Conclusions

Nonlinear bending and forced vibration of GPLRC dielectric beam are investigated by numerically solving governing equations, which are derived based on Timoshenko beam theory and von Kármán geometrical nonlinearity. The analysis demonstrates that there exists a critical GPL concentration, below which the electrical loading has limited effects on nonlinear bending and forced vibration of the composite beam. For higher GPL concentration, it is found that the effects of electrical loading on the structural behaviours of the GPL/PVDF beam comprehensively depend on the thickness of the beam, the GPL aspect ratio and AC frequency. Due to the effects of dielectric property, the increase of GPL concentration results in increase of deflection when the beam is subjected to electrical voltage, which is different from the observation as usually expected. A transition region is observed for the effects of AC frequency. Within this region, the structural performances of the composite beam are very sensitive to the change of the AC frequency. A slight variation in the AC frequency can result dramatic change in the structural behaviours of the composite beam. More parametric study is also conducted on the effects of damping ratio and initial axial stress.

Acknowledgements

The work described in this paper is fully funded by a research grant from the Australian Research Council under Discovery Early Career Researcher Award (DECRA) scheme (DE160100086). The authors

are grateful for the financial support from the Australian Research Council under Discovery Project scheme (DP160101978).

Conflict of Interest

The authors declare no conflict of interests.

Table Captions

Table 1 Dimensionless midpoint deflection of GPLRC beam with different boundary conditions.

Table 2 Comparion of dimensionless midpoint deflections of beams with various loadings.

Figure Captions

Fig. 1. Schematic configuration of GPLRC beam.

Fig. 2. Variation of dimensionless midpoint deflection with thickness of GPL/PVDF beam.

Fig. 3. Variation of dimensionless deflection of GPL/PVDF beam with GPL concentration (a) f_{AC} = 0 Hz; (b) V_{DC} = 50 V.

Fig. 4. Variation of dimensionless midpoint deflection of GPL/PVDF with GPL aspect ratio (a) V_{DC} = 10 V (b) V_{DC} = 20 V (c) V_{DC} = 30 V (d) V_{DC} = 40 V.

Fig. 5. Variation of dimensionless midpoint deflection of GPL/PVDF composite beam with voltage.

Fig. 6. Variation of dimensionless midpoint deflection of GPL/PVDF composite beam with AC frequency.

Fig. 7. Steady-state response of GPL/PVDF composite beam with different beam thicknesses (a) Time history at V_{DC} = 0 V; (b) Time history at V_{DC} = 250V; (c) Phase portrait at V_{DC} = 0 V; (b) Phase portrait at V_{DC} = 250 V.

Fig. 8. Steady-state response of GPL/PVDF beam with different initial axial stresses (a) Time history; (b) Phase portrait.

Fig. 9. Steady-state response of GL/PVDF beam with different damping ratios (a) Time history; (b) Phase portrait.

Fig. 10. Steady-state response of GPL/PVDF beam with different GPL weight fractions (a) Time history at V_{DC} = 0; (b) Time history at V_{DC} = 250 V; (c) Phase portrait at V_{DC} = 0 (d) Phase portrait at V_{DC} = 250 V.

Fig. 11. Steady-state response of GPL/PVDF composite beam with different GPL aspect ratios (a) Time history at V_{DC} = 0; (b) Time history at V_{DC} = 100 V; (c) Phase portrait at V_{DC} = 0; (d) Phase portrait at V_{DC} = 100 V.

Fig. 12. Steady-state response of GPL/PVDF beam subjected to different electrical voltages (a) Time history; (b) Phase portrait.

Fig. 13. Steady-state response of GPL/PVDF beam subjected to different AC frequencies (a) Time history; (b) Phase portrait.

References

[1] T. Chen, J. Qiu, K. Zhu, X. He, X. Kang, E.l. Dong, Poly(methyl methacrylate)-functionalized graphene/polyurethane dielectric elastomer composites with superior electric field induced strain, Mater. Lett. 128 (2014) 19-22.

[2] S. Liu, M. Tian, B. Yan, Y. Yao, L. Zhang, T. Nishi, N. Ning, High performance dielectric elastomers by partially reduced graphene oxide and disruption of hydrogen bonding of polyurethanes, Polymer 56 (2015) 375-384.

[3] A. Javey, H. Kim, M. Brink, Q. Wang, A. Ural, J. Guo, P. McIntyre, P. McEuen, M. Lundstrom, H. Dai, High-kappa dielectrics for advanced carbon-nanotube transistors and logic gates, Nat. Mater. 1 (4) (2002) 241-246.

[4] K. Jung, K.J. Kim, H.R. Choi, A self-sensing dielectric elastomer actuator, Sens. Actuat. A Phys. 143 (2) (2008) 343-351.

[5] C. Feng, L. Jiang, W.M. Lau, Dynamic characteristics of a dielectric elastomer-based microbeam resonator with small vibration amplitude, J. Micromech. Microeng. 21 (9) (2011) 095002-095002.

[6] M. Wissler, E. Mazza, Modeling and simulation of dielectric elastomer actuators, Smart Mater. Struct. 14 (6) (2005) 1396-1402.

[7] C. Feng, L. Yu, W. Zhang, Dynamic analysis of a dielectric elastomer-based microbeam resonator with large vibration amplitude, Int. J. Nonlin. Mech. 65 (2014) 63-68.

[8] M. Selvi, S. Devaraju, K. Sethuraman, M. Alagar, Carbon black-polybenzoxazine nanocomposites for highKdielectric applications, Polym. Compos. 35 (11) (2014) 2121-2128.

[9] C. Calberg, S. Blacher, F. Gubbels, F. Brouers, R. Deltour, R. Jérôme, Electrical and dielectric properties of carbon black filled co-continuous two-phase polymer blends, J. Phys. D Appl. Phys. 32 (13) (1999) 1517-1525.

[10] L. Wang, Z.-M. Dang, Carbon nanotube composites with high dielectric constant at low percolation threshold, Appl. Phys. Lett. 87 (4) (2005) 042903.

[11] A. Ameli, M. Nofar, C.B. Park, P. Pötschke, G. Rizvi, Polypropylene/carbon nanotube nano/microcellular structures with high dielectric permittivity, low dielectric loss, and low percolation threshold, Carbon 71 (2014) 206-217.

[12] J. Ren, D. Yu, L. Feng, G. Wang, G. Lv, Nanocable-structured polymer/carbon nanotube composite with low dielectric loss and high impedance, Compos. Part A Appl. Sci. Manuf. 98 (2017) 66-75.
[13] M. Tian, J. Zhang, L. Zhang, S. Liu, X. Zan, T. Nishi, N. Ning, Graphene encapsulated rubber latex composites with high dielectric constant, low dielectric loss and low percolation threshold, J. Colloid Interf. Sci. 430 (2014) 249-256.
[14] Y. Chen, Q. Zhuang, X. Liu, J. Liu, S. Lin, Z. Han, Preparation of thermostable PBO/graphene nanocomposites with high dielectric constant, Nanotechnology 24 (24) (2013) 245702.
[15] P. Fan, L. Wang, J. Yang, F. Chen, M. Zhong, Graphene/poly(vinylidene fluoride) composites with high dielectric constant and low percolation threshold, Nanotechnology 23 (36) (2012) 365702.
[16] Y.T. Park, Y. Qian, C. Chan, T. Suh, M.G. Nejhad, C.W. Macosko, A. Stein, Epoxy Toughening with Low Graphene Loading, Adv. Func. Mater. 25 (4) (2015) 575-585.
[17] M.A. Rafiee, J. Rafiee, Z.Z. Yu, N. Koratkar, Buckling resistant graphene nanocomposites, Appl. Phys. Lett. 95 (22) (2009) 223103.
[18] X. Zhao, Q. Zhang, D. Chen, P. Lu, Enhanced Mechanical Properties of Graphene-Based Poly(vinyl alcohol) Composites, Macromolecules 43 (5) (2010) 2357-2363.
[19] R. Rahman, A. Haque, Molecular modeling of crosslinked graphene–epoxy nanocomposites for characterization of elastic constants and interfacial properties, Compos. Part B Eng. 54 (2013) 353-364.
[20] R. Sun, L. Li, C. Feng, S. Kitipornchai, J. Yang, Tensile behavior of polymer nanocomposite reinforced with graphene containing defects, Eur. Polym. J . 98 (2018) 475-482.
[21] X.-Y. Ji, Y.-P. Cao, X.-Q. Feng, Micromechanics prediction of the effective elastic moduli of graphene sheet-reinforced polymer nanocomposites, Model. Simul. Mater. Sci. Eng. 18 (4) (2010) 045005.
[22] C. Feng, Y. Wang, J. Yang, Effects of Reorientation of Graphene Platelets (GPLs) on Young's Modulus of Polymer Composites under Bi-Axial Stretching, Nanomaterials 8 (1) (2018) 27.
[23] K. Spanos, S. Georgantzinos, N. Anifantis, Mechanical properties of graphene nanocomposites: A multiscale finite element prediction, Compos. Struct. 132 (2015) 536-544.

[24] C. Feng, Y. Wang, S. Kitipornchai, J. Yang, Effects of Reorientation of Graphene Platelets (GPLs) on Young's Modulus of Polymer Nanocomposites under Uni-Axial Stretching, Polymers 9 (10) (2017) 532.
[25] F. He, S. Lau, H.L. Chan, J. Fan, High Dielectric Permittivity and Low Percolation Threshold in Nanocomposites Based on Poly(vinylidene fluoride) and Exfoliated Graphite Nanoplates, Adv. Mater. 21 (6) (2009) 710-715.
[26] X. Xia, Y. Wang, Z. Zhong, G.J. Weng, A frequency-dependent theory of electrical conductivity and dielectric permittivity for graphene-polymer nanocomposites, Carbon 111 (2017) 221-230.
[27] C. Feng, S. Kitipornchai, J. Yang, Nonlinear free vibration of functionally graded polymer composite beams reinforced with graphene nanoplatelets (GPLs), Eng. Struct. 140 (2017) 110-119.
[28] Y. Kiani, M. Mirzaei, Enhancement of non-linear thermal stability of temperature dependent laminated beams with graphene reinforcements, Compos. Struct. 186 (2018) 114-122.
[29] C. Feng, S. Kitipornchai, J. Yang, Nonlinear bending of polymer nanocomposite beams reinforced with non-uniformly distributed graphene platelets (GPLs), Compos. Part B Eng. 110 (2017) 132-140.
[30] J. Yang, H. Wu, S. Kitipornchai, Buckling and postbuckling of functionally graded multilayer graphene platelet-reinforced composite beams, Compos. Struct. 161 (2017) 111-118.
[31] H. Wu, J. Yang, S. Kitipornchai, Dynamic instability of functionally graded multilayer graphene nanocomposite beams in thermal environment, Compos. Struct. 162 (2017) 244-254.
[32] D. Chen, J. Yang, S. Kitipornchai, Nonlinear vibration and postbuckling of functionally graded graphene reinforced porous nanocomposite beams, Compos. Sci. Technol. 142 (2017) 235-245.
[33] H.-S. Shen, Y. Xiang, F. Lin, Nonlinear bending of functionally graded graphene-reinforced composite laminated plates resting on elastic foundations in thermal environments, Compos. Struct. 170 (2017) 80-90.
[34] H.-S. Shen, Y. Xiang, F. Lin, Nonlinear vibration of functionally graded graphene-reinforced composite laminated plates in thermal environments, Comput. Meth. Appl. Mech. Eng. 319 (2017) 175-193.

[35] R. Gholami, R. Ansari, Large deflection geometrically nonlinear analysis of functionally graded multilayer graphene platelet-reinforced polymer composite rectangular plates, Compos. Struct. 180 (2017) 760-771.
[36] M. Song, S. Kitipornchai, J. Yang, Free and forced vibrations of functionally graded polymer composite plates reinforced with graphene nanoplatelets, Compos. Struct. 159 (2017) 579-588.
[37] Z. Zhao, C. Feng, Y. Wang, J. Yang, Bending and vibration analysis of functionally graded trapezoidal nanocomposite plates reinforced with graphene nanoplatelets (GPLs), Compos. Struct. 180 (2017) 799-808.
[38] B. Yang, S. Kitipornchai, Y.-F. Yang, J. Yang, 3D thermo-mechanical bending solution of functionally graded graphene reinforced circular and annular plates, Appl. Math. Model. 49 (2017) 69-86.
[39] Y. Wang, C. Feng, Z. Zhao, J. Yang, Buckling of Graphene Platelet Reinforced Composite Cylindrical Shell with Cutout, Int. J. Struct. Stab. Dyn. 18 (03) (2018) 1850040.
[40] Y. Wang, C. Feng, Z. Zhao, J. Yang, Eigenvalue buckling of functionally graded cylindrical shells reinforced with graphene platelets (GPL), Compos. Struct. 202 (2018) 38-46.
[41] S. Sahmani, M. Aghdam, A nonlocal strain gradient hyperbolic shear deformable shell model for radial postbuckling analysis of functionally graded multilayer GPLRC nanoshells, Compos. Struct. 178 (2017) 97-109.
[42] Y. Wang, C. Feng, Z. Zhao, F. Lu, J. Yang, Torsional buckling of graphene platelets (GPLs) reinforced functionally graded cylindrical shell with cutout, Compos. Struct. 197 (2018) 72-79.
[43] M.A. Rafiee, J. Rafiee, Z. Wang, H. Song, Z.Z. Yu, N. Koratkar, Enhanced mechanical properties of nanocomposites at low graphene content, ACS Nano 3 (12) (2009) 3884-3890.
[44] G.J. Weng, A dynamical theory for the Mori–Tanaka and Ponte Castañeda–Willis estimates, Mech. Mater. 42 (9) (2010) 886-893.
[45] H. Liu, L.C. Brinson, Reinforcing efficiency of nanoparticles: A simple comparison for polymer nanocomposites, Compos. Sci. Technol. 68 (6) (2008) 1502-1512.
[46] M. Taya, Electronic composites: modeling, characterization, processing, and MEMS applications, Cambridge University Press, 2005.
[47] G.D. Seidel, D.C. Lagoudas, A micromechanics model for the electrical conductivity of nanotube-polymer nanocomposites, J. Compos. Mater. 43 (9) (2009) 917-941.

[48] C. Feng, L. Jiang, Micromechanics modeling of the electrical conductivity of carbon nanotube (CNT)–polymer nanocomposites, Compos. Part A Appl. Sci. Manuf. 47 (2013) 143-149.
[49] Y. Wang, J.W. Shan, G.J. Weng, Percolation threshold and electrical conductivity of graphene-based nanocomposites with filler agglomeration and interfacial tunneling, J. Appl. Phys. 118 (6) (2015) 065101.
[50] Y. Wang, G.J. Weng, S.A. Meguid, A.M. Hamouda, A continuum model with a percolation threshold and tunneling-assisted interfacial conductivity for carbon nanotube-based nanocomposites, J. Appl. Phys. 115 (19) (2014) 193706.
[51] R. Hashemi, G.J. Weng, A theoretical treatment of graphene nanocomposites with percolation threshold, tunneling-assisted conductivity and microcapacitor effect in AC and DC electrical settings, Carbon 96 (2016) 474-490.
[52] J.C. Dyre, A simple model of ac hopping conductivity in disordered solids, Phys. Lett. A 108 (9) (1985) 457-461.
[53] R.K. Layek, S. Samanta, D.P. Chatterjee, A.K. Nandi, Physical and mechanical properties of poly(methyl methacrylate) -functionalized graphene/poly(vinylidine fluoride) nanocomposites: Piezoelectric β polymorph formation, Polymer 51 (24) (2010) 5846-5856.
[54] A.H. Nayfeh, M.I. Younis, E.M. Abdel-Rahman, Dynamic pull-in phenomenon in MEMS resonators, Nonlinear Dynam. 48 (1-2) (2006) 153-163.
[55] X. Wang, Differential quadrature and differential quadrature based element methods: theory and applications, Butterworth-Heinemann, 2015.
[56] S.M. Ibrahim, B.P. Patel, Y. Nath, Modified shooting approach to the non-linear periodic forced response of isotropic/composite curved beams, Int. J. Nonlin. Mech. 44 (10) (2009) 1073-1084.
[57] J.N. Reddy, S. El-Borgi, J. Romanoff, Non-linear analysis of functionally graded microbeams using Eringen′s non-local differential model, Int. J. Nonlin. Mech. 67 (2014) 308-318.